UNIVERSITÀ
DI PAVIA

UNIVERSITY OF PAVIA

FACULTY OF ENGINEERING

DEPARTMENT OF ELECTRICAL, COMPUTER AND BIOMEDICAL ENGINEERING

MASTER'S DEGREE IN ELECTRICAL ENGINEERING

MASTER THESIS

"Investigation on unbalanced conditions in Induction Motors through a digital moulded-case circuit breaker"

"Analisi delle condizioni di sbilanciamento nei motori a induzione mediante un interruttore automatico digitale scatolato"

Candidate: Mohammad Junaid

Supervisor: Prof. Lucia Frosini

Co- Supervisor: Dr. Marcello Minervini

A.A. 2024/2025

First of all, thanks to Almighty ALLAH.

I would like to take this opportunity to thank Prof. Lucia Frosini for the invaluable opportunity to work under his guidance as I approach the end of my thesis and, consequently, my master's journey. My thesis and subsequent academic endeavours have been greatly influenced by his resolute assistance, inspiration, and knowledge.

My sincere gratitude also goes out to Dr. Marcello Minervini, whose assistance and wisdom have been invaluable to the accomplishment of my project. I am grateful to have had the chance to work with such a gifted and encouraging colleague; his advice, tolerance, and willingness to impart his knowledge have been priceless.

In addition, I want to thank the University of Pavia faculty as a whole for their unwavering encouragement and support during my academic career. The members' varied viewpoints and proficiencies have enhanced my educational journey and made a substantial contribution to both my career and personal development.

Finally, but most importantly, I would like to thank my family and friends for their unwavering support and motivation. My motivation has come from your encouragement, and I appreciate your patience and understanding during this academic endeavour's difficult times.

As this chapter of my academic life draws to an end, I consider the profound influence each of you has had on my path. I sincerely appreciate all of the advice, understanding, and assistance that helped to mold my thesis and improve my educational journey as a whole.

Contents

Abstract

This thesis examines the impact of supply voltage unbalance on three-phase induction motors, with emphasis on its effect on current and voltage signal based diagnostic indicators. Experimental tests were performed on a laboratory setup under controlled load and unbalanced voltage conditions, using conventional instrumentation and a digital moulded-case circuit breaker.

The acquired signals were analysed in MATLAB through frequency-domain techniques, including FFT and harmonic evaluation. The results show that even minor voltage unbalance leads to significant current distortion and alters harmonic components commonly used for fault detection namely the supply third harmonic. However, having the three phase currents, and not only one, permitted to observe differences between them.

As regards the voltage signals, interesting observations are obtained: third harmonic of the voltage is still interested in changes in unbalance conditions and particular inter-harmonics are found sensitive. Moreover, it has been noticed the presence of these harmonics only in two of the three phase-to-phase voltages; this permits the localization of the defect that give the voltage unbalance (e.g. a high resistance connection in one phase).

Introduction

The reliable operation of three-phase induction motors is of fundamental importance in modern industrial systems, where they represent the backbone of electromechanical energy conversion. Despite their robustness and widespread use, induction motors are highly sensitive to power quality issues, among which supply voltage unbalance is one of the most common and detrimental. Even relatively small deviations from balanced conditions can lead to significant performance degradation, increased losses, overheating, and accelerated aging of machine components.

In this context, condition monitoring techniques play a crucial role in ensuring system reliability and enabling predictive maintenance strategies. Among these techniques, Motor Current Signature Analysis (MCSA) has gained significant attention due to its non-intrusive nature and its capability to detect a wide range of electrical and mechanical faults through spectral analysis of stator currents. However, the presence of voltage unbalance can influence the harmonic content of the current signals, potentially affecting the reliability and interpretation of diagnostic indicators.

The main objective of this thesis is to investigate the effects of supply voltage unbalance on induction motor behaviour, with particular focus on harmonic components used in MCSA. The study also explores the potential of integrating advanced protection devices, such as digital moulded-case circuit breakers, into the diagnostic framework, thereby combining protection and monitoring functionalities within a single system.

To achieve these objectives, a dedicated experimental test bench was developed, consisting of a three-phase induction motor coupled with a magnetic powder brake to simulate different load conditions. Controlled voltage unbalance was introduced through a rheostat connected to one phase, allowing systematic analysis under various operating scenarios. Electrical quantities, including currents and voltages, were acquired using both conventional measurement systems and an ABB digital circuit breaker equipped with the Ekip Connect platform.

The acquired signals were processed using MATLAB through a structured methodology including time-domain analysis, calculation of voltage and current unbalance, frequency-domain analysis via Fast Fourier Transform (FFT), harmonic evaluation, phase angle extraction, and Total Harmonic Distortion (THD) assessment.

Through this work, a deeper understanding of the interaction between voltage unbalance and harmonic signatures is achieved, contributing to the improvement of diagnostic techniques for induction motors.

Chapter 1: Induction motor Diagnostics and the problem of voltage unbalance.

1.1 The Spread of Electrical Machine Condition Monitoring and Diagnostics

1.1.1 Introduction

A key component of contemporary industrial productivity, efficiency, and safety is the dependable operation of industrial electric motors and generators. The field of condition monitoring and diagnostics has developed from simple offline inspections to a sophisticated discipline utilising a spectrum of cutting-edge, complementary tools to protect these vital assets. Enabling a predictive maintenance paradigm is the major objective, going beyond planned or reactive operations to a data-driven strategy that minimises lifecycle costs and guarantees operational continuity [1]. The main justifications for implementing these technologies are presented in this chapter, along with the advantages and complementary features of the different diagnostic techniques.

1.1.2 The critical role of insulation health assessment

One of the main goals of condition monitoring is to evaluate the electrical insulation system, which has been repeatedly found to be a major contributor to machine failure in industrial surveys. Over time, thermal, mechanical, and electrical stressors cause the organic elements in insulation to deteriorate. With the major benefit of evaluating insulation integrity under real-world operating conditions, online partial discharge (PD) monitoring has become the most popular method for this purpose in medium voltage machines.

Partial Discharges (PD) are localised electrical discharges that only incompletely span the insulation between conductors. They occur in regions of the insulation system that are subjected to high electrical stress, such as voids, cavities, or sharp imperfections. These discharges do not cause immediate, complete breakdown but represent a gradual degradation process, where cumulative erosion of the material can eventually lead to a full insulation failure.

Online partial discharge (PD) monitoring allows for a realistic health assessment without requiring shutdown [1]. Even while noisy settings provide difficulties, continued research into sophisticated noise separation and AI-powered pattern recognition has potential for improving dependability even more, especially for contemporary inverter-fed motors that use Wide Bandgap (WBG) semiconductors [1].

Condition monitoring of machine insulation began with medium voltage machines. These machines have much more electrical insulation between turns, phases and from phases to ground. These machines, with higher voltage levels (phase to phase voltage can reach 20 kV), can be subjected to partial discharges when the insulation has some defects or is across its aging process. This kind of machinery have a form-wound windings, i.e. the turns are located

ordinately to keep low and fixed the turn-to-turn voltage. This kind of winding is represented in Fig 1.1.

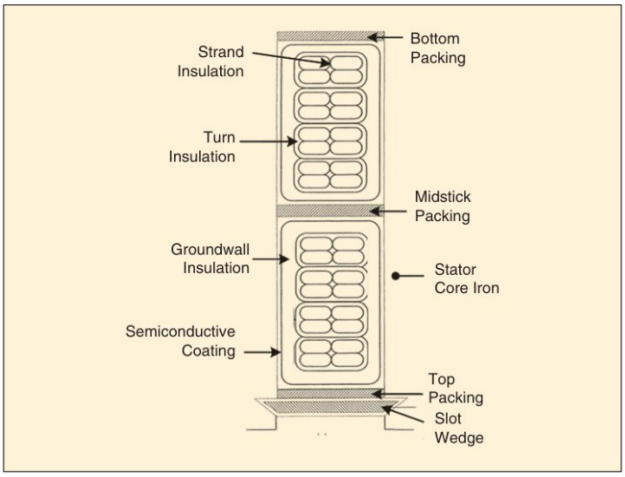

Fig 1.1: A cross-section of a slot containing strand, turn, phase and Ground Wall insulation components in a multiturn form of wound stator coil [1].

As mentioned above, the machines fed with electronic converters, especially the high-speed switching devices i.e. WBG, are subjected to insulation stress even at low voltages (400 V or even less). These machines are with random-wound winding, i.e. a winding composed of many enamelled round wires distributed randomly inside the stator slots; in this case the voltage between two wires (the turn-to-turn voltage) can be of few volts or of higher values depending if the adjacent wires are of successive turns or not. A random wound winding, during manufacturing process, is represented in the next image.

Fig 1.2: Typical Random-Wound Winding being inserted into a stator slot [6].

The insulation condition monitoring can be conducted online or offline. In the first case the analysis is conducted while the machine is in operation while the second requires a stop of the machine. Some techniques of insulation condition monitoring are presented in [1].

1.1.3 Motor Current Signature Analysis: A Pillar of Non-Intrusive Monitoring

One of the most popular and useful methods in the condition monitoring toolbox is Motor Current Signature Analysis (MCSA). Its unique benefits, which include being essentially non-intrusive, avoiding the need to place more sensors on the machine, and allowing for low-cost remote monitoring by leveraging current measurements, are what propel its extensive use [1].

Motor Current Signature Analysis (MCSA) relies on measuring and analysing the stator current to detect electrical and mechanical faults within an electric machine. The basic setup for this technique is illustrated in the following figure. It consists of current sensors (usually current transformers or Hall-effect sensors), a signal acquisition unit, and a data processing system that performs spectral analysis to identify characteristic fault frequencies.

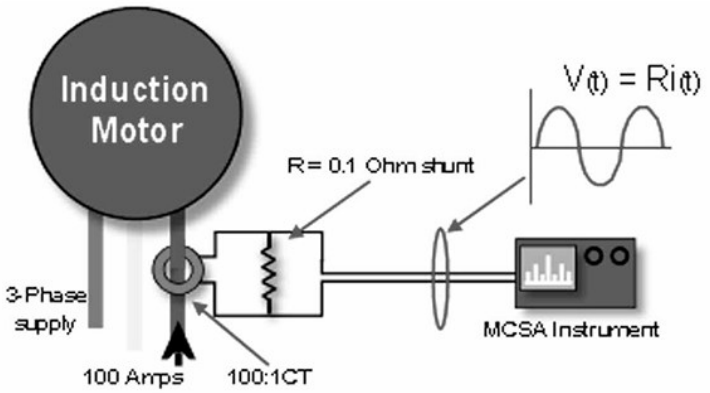

Fig 1.3: Basic MCSA Instrumentation System [3].

MCSA has demonstrated remarkable efficacy in identifying fault conditions. Its ability to accurately identify broken rotor bars in induction motors by examining distinctive sidebands in the current spectrum is its most noteworthy accomplishment. Early fault identification is made possible by this capability, which gives enough notice to plan maintenance and avoid unplanned downtime. The fundamental tenet of the approach, which states that errors appear as predictable variations in the stator current, offers a flexible diagnostic framework. To improve MCSA's diagnostic accuracy and dependability in a wider range of operating situations, ongoing research is actively extending its capabilities, especially through integration with sophisticated signal processing and intelligent algorithms [1].

1.1.4 MCSA: The Fault of Broken Rotor Bars

The detection of broken rotor bars (BRB) is one of the most established applications of MCSA. The underlying mechanism stems from the induction of a backward-rotating magnetic field at slip frequency in the rotor when an asymmetry, such as a broken bar, is present [3].

When a rotor bar in an induction motor is broken, an asymmetry is introduced into the rotor circuit. This asymmetry causes the generation of a backward-rotating magnetic field at the slip

frequency, in addition to the normal forward-rotating magnetic field that produces torque. The interaction between these two fields creates additional frequency components in the stator current, which appear as sidebands around the fundamental supply frequency.

The slip (s) is a critical parameter and is calculated from the motor's actual speed (N_r) and synchronous speed (N_s):

$$s = \frac{N_s - N_r}{N_s}$$

When a non-symmetric current flows in the bars, due to an interruption of one or more of them, the magnetic field assumes a non-sinusoidal distribution. While a rotating sinusoidal distribution is composed only by the forward rotating component, a non-symmetrical distribution can be decomposed into forward and reverse rotating components.

The following figure illustrates the concept: the forward-rotating field corresponds to the normal torque-producing flux, while the backward-rotating field arises due to the rotor asymmetry caused by the broken bar.

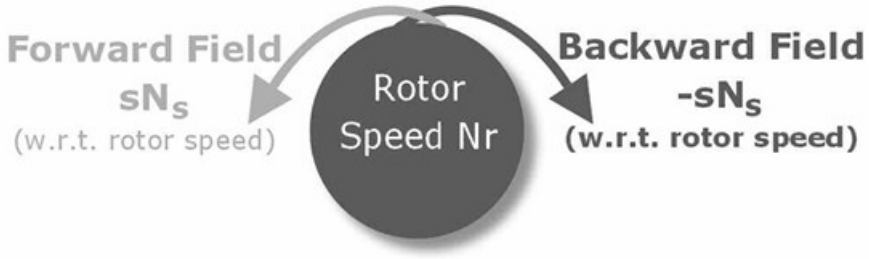

Fig 1.4: Illustration of Forward and Backward Rotating Fields from Rotor Currents when a Broken Bar exists [3].

This reverse-rotating field induces specific current components in the stator windings. Since the rotor forward field rotates synchronously with the stator field but the rotor rotates at speed $N_R = N_s - N_s \cdot s$, the harmonics induced by the backward field are at:

$$f_b = f_s(1 - 2s)$$

Where f_s is the electrical supply frequency.

Due to speed ripples induced by the torque ripples generated by the non-symmetric field, two components manifest as sidebands around the supply frequency (f_s) in the current spectrum, given by the equation [18]:

$$f_b = f_s(1 \pm 2s)$$

The severity of the fault can be estimated by the magnitude of these sidebands relative to the fundamental supply frequency, often expressed in decibels (dB). A significant increase in the sideband's amplitude indicates a worsening condition.

The next figure compares the stator current spectra of an induction motor under healthy conditions and with a broken rotor bar. In the healthy motor, the current spectrum contains a single dominant peak at the supply frequency. However, when one or more broken bars are present, the two additional sideband components emerge. The relative amplitude of these sidebands with respect to the main peak provides a reliable indication of the extent of rotor damage.

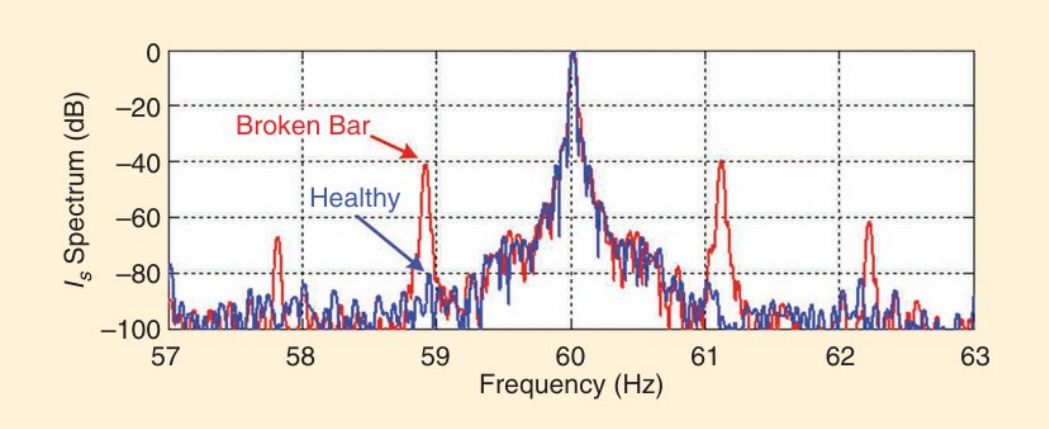

Fig 1.5: Stator Current spectra of an Induction Motor with and without a broken rotor bar[1].

Industrial experience confirms the theoretical principles discussed above. Moreover, when broken rotor bars occur, the resulting asymmetry in the rotor cage not only modifies the electromagnetic field distribution but also leads to visible mechanical and thermal effects on the rotor surface. Specifically, the bars adjacent to the broken one are subjected to an increase in current density, since they carry the current that the broken bar does not carry due to the fracture. So, because of this stress the adjacent bars can collapse themselves increasing the fault extension to a very severe state. The following figure shows an actual example of a broken rotor bar fault observed in an industrial motor.

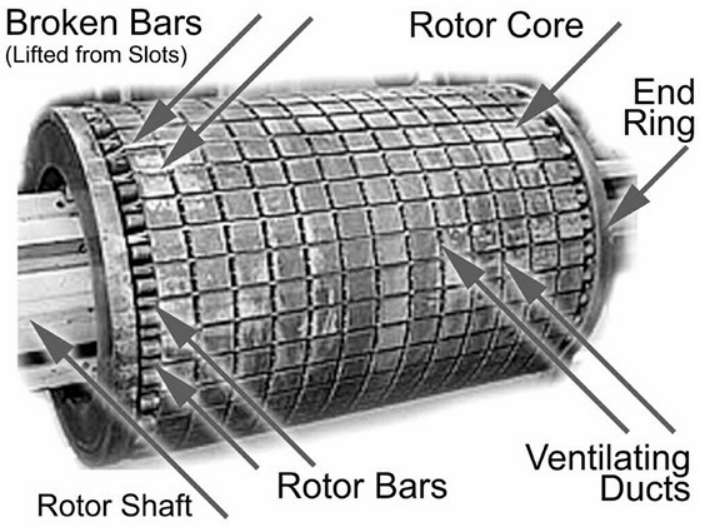

Fig 1.6: An example of Broken Rotor Bar problem [3].

In the case analysed in [3], several adjacent bars have fractured due to excessive thermal and mechanical stress caused by repeated high-torque start-ups. Such damage leads to localized overheating, loss of torque, and increased vibration [3]. As said before, in this case the fault has propagated to neighbouring bars and eventually result in catastrophic rotor failure, because of debris release in the airgap. Early identification through Motor Current Signature Analysis allows operators to schedule maintenance before the fault escalates to a complete breakdown.

1.1.5 MCSA: Other Faults

In addition to broken rotor bars, MCSA can detect a wide array of other faults, each producing a unique signature in the current spectrum:

- **Stator Winding Faults:** The integrity of the stator winding is paramount for reliable motor operation. These faults often begin as minor insulation degradation between turns in a single coil, known as inter-turn short circuits. When a short circuit occurs, it creates an imbalance in the magnetic fields within the stator slots. This imbalance manifests as specific harmonic components in the stator current spectrum. According to [1], these are typically odd harmonics of the supply frequency, particularly the 3^{rd}, 5^{th}, and 7^{th} harmonics. The fundamental principle is that the faulty winding creates a small, localized magnetic asymmetry, which modulates the main flux and induces these characteristic frequencies in the current. Early detection of these signatures is necessary, as it allows for intervention before the fault escalates into a catastrophic phase-to-phase or earth fault, which would require extensive and costly repairs [1, 3]. The fault development is very rapidly (much more than the broken rotor bars) and from incipient to catastrophic stages only a few minutes may pass.
  The next figure shows an example of mechanical and thermal damage to a high-voltage stator winding resulting from such insulation failure**.** Deformed and discoloured coils are visible in the image, evidence of overheating caused by arcing and electrical stress concentration. This type of damage underscores the importance of early detection through techniques like Motor Current Signature Analysis (MCSA), which can identify characteristic current harmonics before the insulation breakdown reaches this destructive stage.

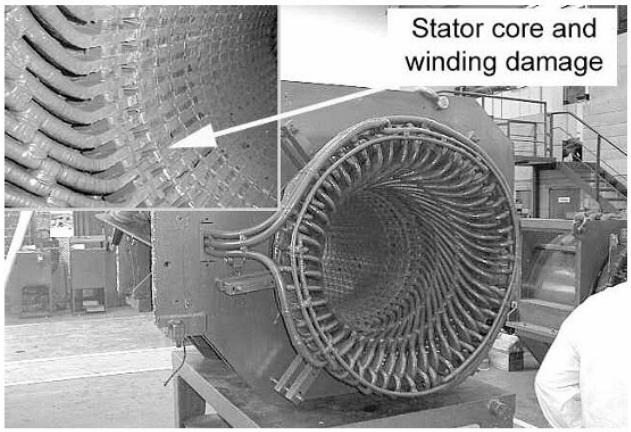

Fig 1.7: Mechanical damage to High Voltage Stator Winding [3].

- **Airgap Eccentricity:** A uniform airgap between the rotor and stator is essential for balanced magnetic forces and smooth operation. Airgap eccentricity occurs when this airgap is non-uniform. This condition is categorized as either static eccentricity (where the rotor is offset from the stator centre but rotates on its own axis) or dynamic eccentricity (where the rotor centre is not at the centre of rotation, creating a "wobble"). In practice, a mixed eccentricity, containing both static and dynamic components, is often present. Abnormal levels of eccentricity produce a characteristic pattern of components around the rotor slot passing frequency (f_{rsp}) and its harmonics in the current spectrum. The fault frequencies can be described by [3]:

$$f_{ecc} = f_s[k(\frac{R}{p}(1-s)) \pm n_{os}]$$

where R is the number of rotor slots, p is the number of pole pairs, s is the slip, $n_{os} = 1,3,\ldots$, and $k = 1,2,3,\ldots$. This signature can diagnose underlying mechanical issues such as stator core ovality, rotor misalignment, worn bearings, or mechanical resonance at twice the supply frequency, often excited by voltage unbalance. Monitoring these components allows for maintenance to be scheduled before the eccentricity progresses to a destructive rotor-stator rub, which can cause severe damage to the core and windings [1, 3]. The following pictures mirror the eccentricity parameters representation in a machine and the characteristic harmonics in the stator current spectrum.

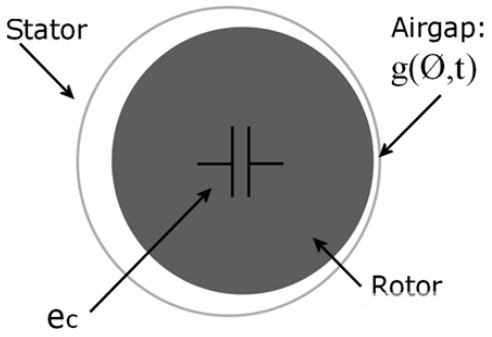

Fig 1.8: Illustration of Airgap Eccentricity [3].

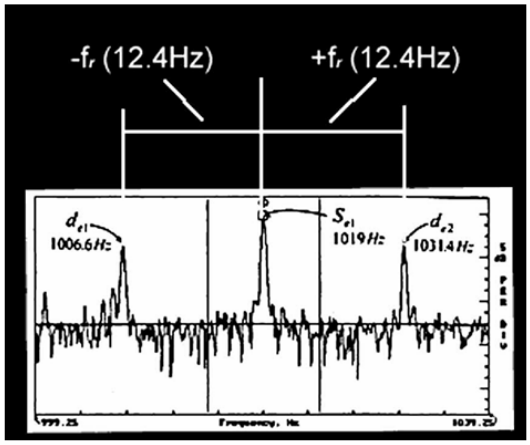

Fig 1.9: Current Spectrum, Unacceptable level of Airgap Eccentricity [3].

- **Bearing Faults:** While vibration analysis is the traditional method for bearing diagnostics, MCSA provides a valuable and complementary approach. Bearing defects such as pits, spalls, or cracks in the inner race, outer race, or rolling elements create specific mechanical vibrations. These vibrations modulate the air-gap length and, consequently, the machine's magnetic field. This modulation transfers to the stator current, generating characteristic fault frequencies side banded around the supply frequency and its harmonics [1, 3].
  The fundamental frequencies associated with bearing failures are a function of the bearing's geometry and rotational speed. These can be calculated for the outer race, inner race, and ball element. MCSA can identify these characteristic frequencies, allowing for the diagnosis of incipient bearing wear. For instance, a defect on the outer race typically produces a frequency component at f_{outer}, calculated as:

$$f_{outer} = f_r \pm k\frac{N}{2} f_r \left(1 - \frac{D_b}{D_c}\cos\beta\right)$$

  where f_r is the rotational frequency, N is the number of rolling elements, D_b is the diameter of the rolling element, D_c is the pitch diameter of the bearing, β is the contact angle between the rolling element and the races and k is the defect constant. The appearance and subsequent growth in the amplitude of these components in the current spectrum serve as a reliable indicator of bearing degradation, enabling maintenance to be planned before complete failure causes secondary damage [3].

- **Summary of the characteristic harmonics**

  All the fault characteristics harmonics are resumed in the next Fig: 1.10

FAULT (COMPONENT)	CHARACTERISTIC FAULT FREQUENCY
Static eccentricity	$\left[kR\left(\frac{1-s}{p}\right)\pm n\right]f_s$
Dynamic and mixed eccentricity	$\left[(kR\pm n_d)\left(\frac{1-s}{p}\right)\pm n\right]f_s$
Mixed eccentricity, PM demagnetization, SM open damper, and shorted field	$nf_s\pm kf_r=\left[n\pm k\frac{(1-s)}{p}\right]f_s$
IM broken rotor bars and end rings	$\left[\frac{k}{p}(1-s)\pm s\right]f_s$
Bearing outer race	$f_s\pm k\frac{N}{2}f_r\left(1-\frac{D_b}{D_c}\cos\beta\right)$
Bearing inner race	$f_s\pm k\frac{N}{2}f_r\left(1+\frac{D_b}{D_c}\cos\beta\right)$
Bearing ball element	$f_s\pm k\frac{D_c}{D_b}f_r\left[1-\left(\frac{D_b}{D_c}\cos\beta\right)^2\right]$

f_s: fundamental frequency, f_r: rotor rotational frequency, s: rotor slip, p: number of pole pairs, R: number of rotor slots, k: integer (= 1, 2, 3, …), n: harmonic order (= 1, 3, 5, …), n_d: dynamic eccentricity order, N: number of balls, D_b: ball diameter, D_c: ball pitch diameter, β: ball contact angle.

Fig 1.10: The characteristic fault frequency components produced by faults in Induction and Synchronous motor [1].

1.2 Introduction to the Problem of Supply Voltage Unbalance

1.2.1 Introduction

Three-phase induction motors are essential in contemporary industry, valued for their durability, reliability, and efficiency. Their performance and operational lifespan, however, are intrinsically linked to the quality of the electrical supply. Among the most prevalent and detrimental power quality issues in electrical systems is supply voltage unbalance [2]. This condition arises when the three-phase voltages at the motor terminals are not equal in magnitude or are not displaced by exactly 120 degrees. Even a slight voltage unbalance can lead to a significant degradation in motor performance, increased losses, and accelerated aging, posing a serious threat to system reliability and operational economics.

1.2.2 The Symmetrical Components Framework

The analytical basis for comprehending unbalanced operation in polyphase systems is the method of symmetrical components, as presented by Fortescue [15]. This powerful technique

resolves an unbalanced three-phase system into three sets of balanced sequence components. An unbalanced set of phase voltages (V_1, V_2, V_3) can be mathematically decomposed into positive-sequence (V_d), negative-sequence (V_i), and zero-sequence (V_o) components using the following transformation:

$$\begin{bmatrix} V_0 \\ V_d \\ V_i \end{bmatrix} = \frac{1}{3} \begin{bmatrix} 1 & 1 & 1 \\ 1 & a & a^2 \\ 1 & a^2 & a \end{bmatrix} \begin{bmatrix} V_1 \\ V_2 \\ V_3 \end{bmatrix}$$

Where $a = e^{j\frac{2}{3}\pi} = -\frac{1}{2} + j\frac{\sqrt{3}}{2}$ is the complex operator that facilitates 120^o phase shift.

Positive-Sequence Components (V_d): A balanced three-phase system with the same phase sequence as the original supply. This component produces the useful forward-rotating magnetic field responsible for the motor's normal torque.

Negative-Sequence Components (V_i): A balanced three-phase system with the opposite phase sequence. This component induces a reverse-rotating magnetic field in the motor.

Zero-Sequence Components (V_0): Three phasors equal in magnitude and phase. In wye-connected systems with an isolated neutral (a common configuration for motors), these components are typically absent.

1.2.3 Detrimental Effects on Induction Motor Operation

When an induction motor is subjected to unbalanced voltages, the negative-sequence component has particularly severe consequences. While the positive-sequence component operates with a slip of "s" and produces the dominant motoring torque, the negative-sequence component, rotating in the opposite direction relative to the rotor, operates at a high slip of "$2 - s$" [2]. This leads to several critical issues:

Increased Currents and Copper Losses: The negative-sequence impedance of the motor is relatively low, meaning that a small negative-sequence voltage (V_i) can cause a large negative-sequence current to flow. The superposition of positive- and negative-sequence currents leads to a significant increase in the current in at least one phase. Since copper losses are proportional to the square of the current ($P_{cu} = I^2R$), this results in excessive heating within the stator and rotor windings.

The temperature rise in the windings is not linear; it can be exponentially related to the voltage unbalance. For example, a 3% voltage unbalance can lead to an ~18% temperature rise, and a 5% unbalance can cause a 50% temperature rise. This dramatically shortens insulation life, as its average life expectancy halves with every 10°C temperature increase [4].

Torque Pulsations and Reduced Average Torque: The electromagnetic torque is produced by the interaction of the air-gap flux and the rotor currents. The positive-sequence system

produces a steady torque, T_e^+ . The negative-sequence system produces a torque, T_e^- , which is negative (braking) in nature. The interaction between the two counter-rotating fields produces a pulsating torque at twice the supply frequency. For example, in three-phase motors fed at 50 Hz, the pulsating torque will be at 100 Hz, while for the motors fed at 60Hz, pulsations occur at 120 Hz. The total instantaneous torque can be expressed as:

$$T_e(t) = T_{avg} + T_{plus}\cos(2\omega t + \varphi)$$

where T_{avg} is the reduced average torque and T_{plus} is the amplitude of the torque pulsation , given the pulsation $\omega = 2\pi f$ and initial phase angle φ [2,5]. To maintain the same mechanical load, the motor must draw more current, further exacerbating the heating problem.

Derated Performance and Efficiency Loss: Voltage unbalance has direct operational consequences that markedly diminish a motor's performance and efficiency. The presence of a negative-sequence voltage component causes a corresponding negative-sequence current to flow. This current does not contribute to useful torque production but instead circulates within the machine, generating substantial additional I^2R losses in the stator and rotor windings [2, 4]. This results in excessive and uneven heating, which is critically important as the average life expectancy of the electrical insulation is halved with every 10°C temperature increase [4].

To avert irreversible insulation failure due to thermal overstress, the motor must be derated, it cannot be safely operated at its full nameplate load. The required derating is severe; for instance, a voltage unbalance of just 3% can cause an approximately 18% temperature rise, necessitating a significant reduction in mechanical load, as per standard derating guidelines [4]. This represents a direct loss of the motor's productive capacity. The overall drive system efficiency also plummets, as a much larger portion of the input electrical power is wasted as heat instead of being converted into useful mechanical work. Studies confirm that system efficiency can be reduced by 20% or more under such unbalanced voltage conditions [5]. The derating factors are expressed in Fig 1.11.

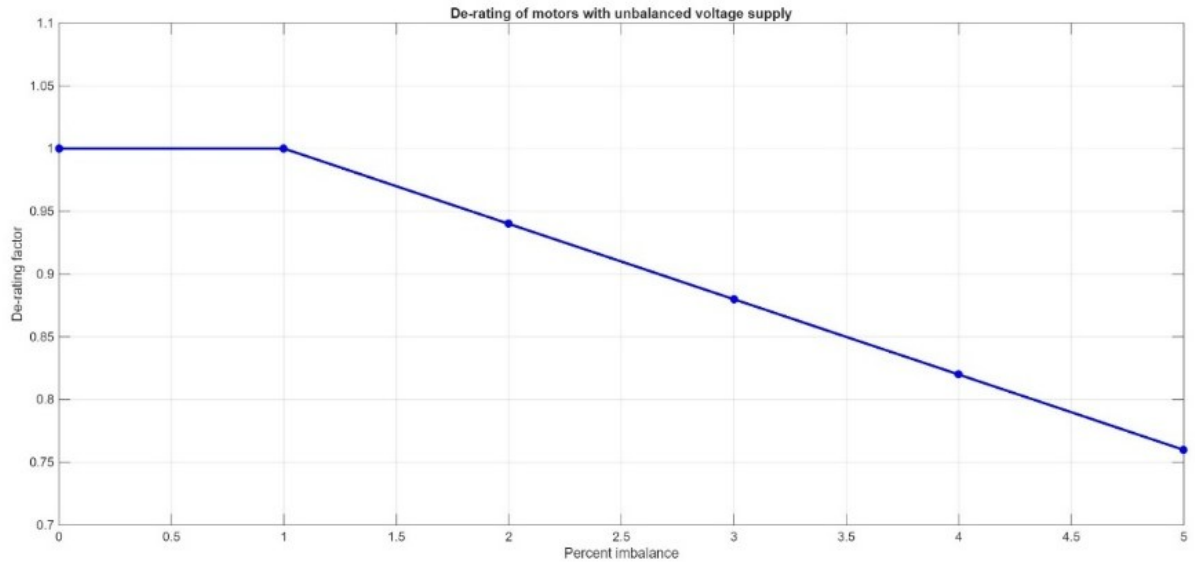

Fig 1.11: Derating of Motors with unbalanced voltage supply [4].

Harmonic Distortion: As demonstrated experimentally [2], unbalanced operation can lead to an increase in current harmonics. Their results showed a notable rise in the 3rd harmonic component under unbalanced supply conditions, which increases the Total Harmonic Distortion (THD) and further degrades power quality, leading to additional losses and potential interference with control electronics [5].

The next figure shows the current harmonic spectrum of a motor supplied by a balanced three-phase voltage. As observed, the waveform remains nearly sinusoidal, and harmonic distortion is minimal, with only small harmonic components visible.

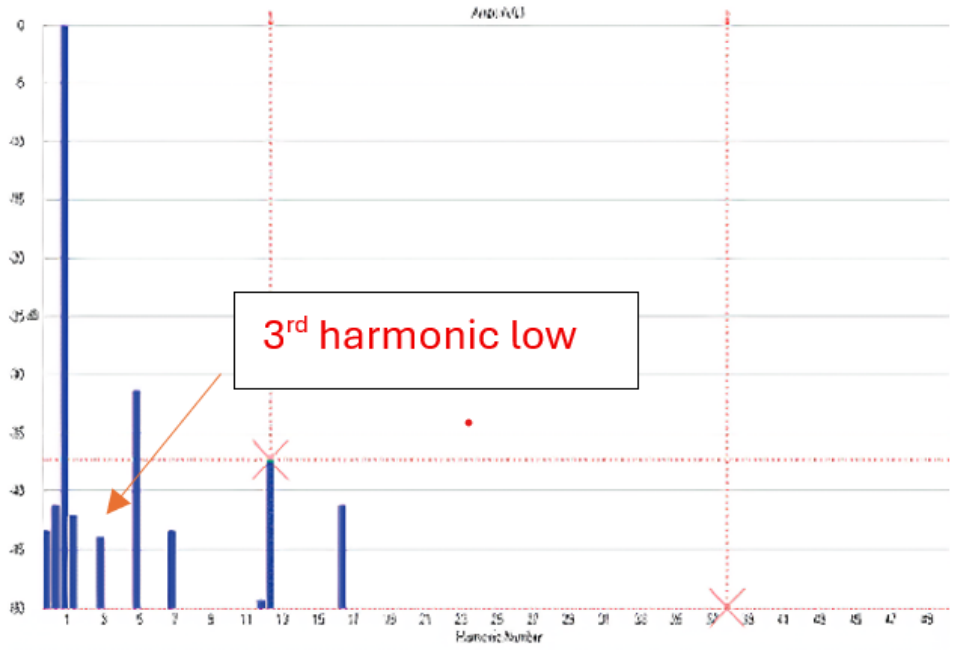

Fig 1.12: Current harmonic spectrum for balanced power supply [2].

In contrast, the following figure depicts the current harmonic spectrum under an unbalanced power supply. Here, the 3rd harmonic and its multiples (specifically the 15th harmonic) become much more pronounced, causing a substantial increase in THD. This confirms that voltage unbalance not only affects thermal and torque performance but also introduces additional electrical distortion that reduces overall system efficiency and reliability.

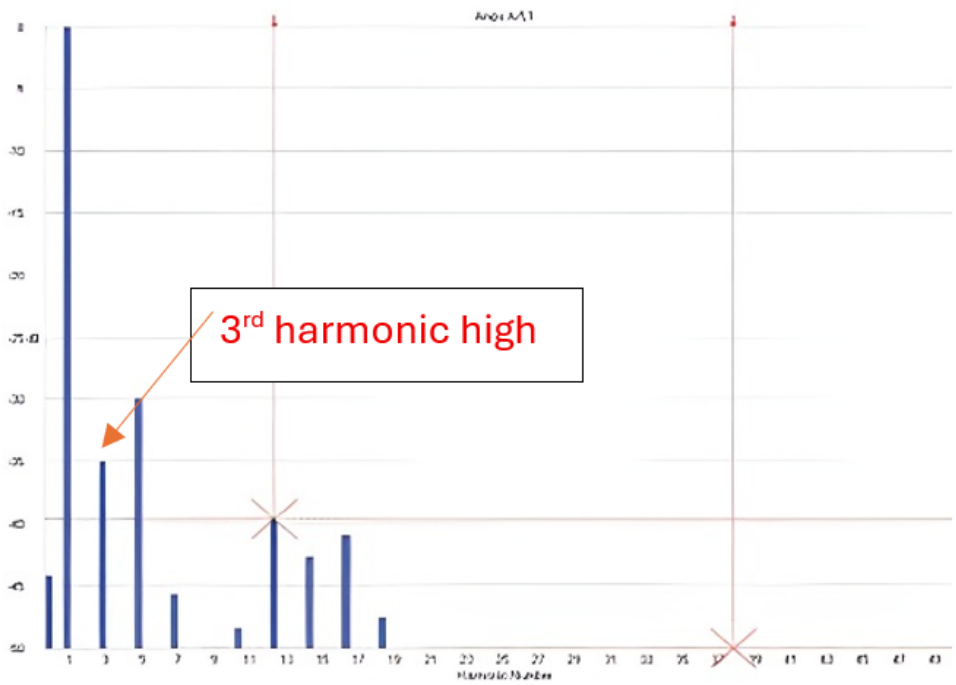

Fig 1.13: Current harmonic spectrum for unbalanced power supply [2].

Mechanical Stress: Voltage unbalance induces significant mechanical stress through the generation of pulsating electromagnetic torques. The interaction between the positive and negative-sequence magnetic fields produces a dominant torque oscillation at twice the supply frequency (e.g., 100/120 Hz) [2]. When combined with supply harmonics, additional high-frequency torque pulsations are superimposed, creating a complex and damaging stress profile [5].

These torque pulsations are transmitted directly through the motor's shaft and bearings. This subjects the entire drive train to cyclic stresses, leading to mechanical fatigue and premature bearing failure over the long term. Furthermore, the negative-sequence component creates an unbalanced magnetic pull (UMP), which can lead to a rotor-stator rub in severe cases, resulting in catastrophic damage to the motor core and windings.

Impact on Drives and Rectifiers: Unbalanced voltage supplies also negatively affect the power electronics that drive and control motors. In Variable Speed Drives (VSDs), voltage unbalance causes increased AC line currents, a 100 Hz ripple on the DC bus, and an increase in reactive power. This can lead to VSD trips on overcurrent or DC bus undervoltage faults. For diode rectifiers, unbalance distorts the normal double-pulse current waveform into a larger single-pulse shape, increasing the current stress on diodes and capacitors, generating excessive heat, and producing uncharacteristic harmonics which are odd multiples of the third harmonic (3^{rd}, 9^{th}, etc.) [4]. Current graphs from balanced and unbalanced conditions in rectifiers are in the next Fig 1.14 and Fig 1.15.

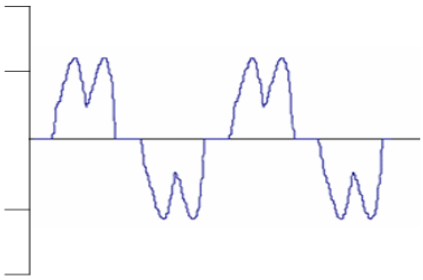

Fig 1.14: Normal line current for one-phase of a three-phase rectifier [4].

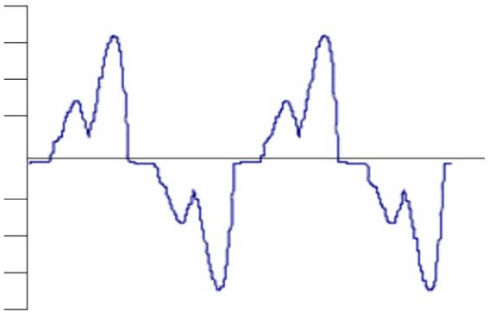

Fig 1.15: Line current with 5% voltage unbalance [4].

1.2.4 Magnitude unbalance and phase unbalance

Further insight into the impact of voltage unbalance on induction motor performance was provided by Khoobroo *et al.* [5], who conducted extensive experimental and simulation-based tests to distinguish between the effects of magnitude unbalance and phase unbalance. Their research demonstrated that these two types of unbalances affect motor behaviour differently.

In the case of magnitude unbalance, where the phase voltages differ in amplitude but maintain a 120° phase displacement, the primary consequence is an uneven distribution of current among the stator phases. This leads to increased copper losses and localized overheating in the most heavily loaded phase.

In contrast, phase unbalance where the voltage magnitudes remain equal but the phase displacement deviates from the ideal 120° was found to cause more severe torque oscillations and efficiency loss. Khoobroo *et al.* observed that even small phase deviations produced significant pulsating electromagnetic torque and negative-sequence currents, resulting in additional mechanical stress and reduced overall motor efficiency.

The following figure, adapted from [5], illustrates the decomposition of the torque components and the corresponding drop in efficiency under unbalanced supply conditions. The steady torque component represents useful mechanical output, while the oscillating components increase with the level of voltage unbalance, causing power pulsations and vibration. The figure clearly shows how the efficiency decreases as the magnitude of unbalance or phase deviation increases.

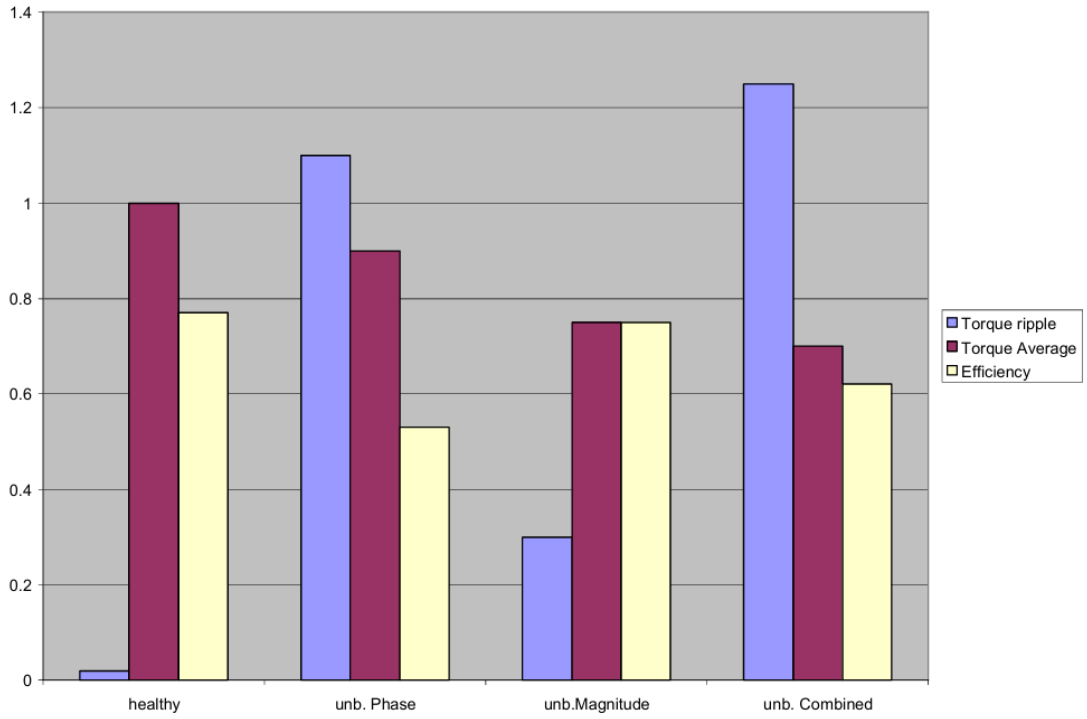

Fig. 1.16: Torque components and efficiency of an induction motor under unbalanced voltage conditions [5].

These findings emphasize that not all forms of voltage unbalance have the same impact. Phase unbalance produces a more harmful effect on both the electromagnetic and mechanical performance of induction machines. Therefore, distinguishing between these two types of unbalances is essential for accurate diagnosis and proper derating in industrial applications.

Chapter 2: Instrumentation and Test Bench

2.1 Introduction

This chapter details the design and components of the dedicated test bench used for this thesis. The primary objective is to use a flexible platform capable of simulating specific motor faults under varying operational loads, while acquiring high-fidelity stator current and other corroborative sensor data. The rigorous utilization of this instrumentation system is critical to ensure the reliability of the data upon which all subsequent analysis and fault diagnosis conclusions will be based.

2.2 Three Phase Asynchronous Motor

A three-phase, squirrel-cage induction motor was selected as the Machine Under Test (MUT) due to its overwhelming prevalence in industrial applications. Its specifications, detailed in Table x, were chosen to provide a relevant power rating for an accurate measure with the circuit breaker used (described later).

Table 2.1: Specifications of the Induction Motor Under Test.

Parameter	**Specification**
Motor Type	3-Phase, Squirrel Cage
Model	1LA71304AA10-Z
Power Rating	5.5kW
Rated Voltage	230/400V
Rated Current	19.8/11.4A
Rated Speed	1455 rpm
Number of Poles	4
Supply Frequency	50 Hz
Rated Torque	36.1Nm
Power Factor	0.81

The next images show the motor label and the frontal and lateral view of the test bench.

Figure 2.1: Motor parameter nameplate from Manufacturer.

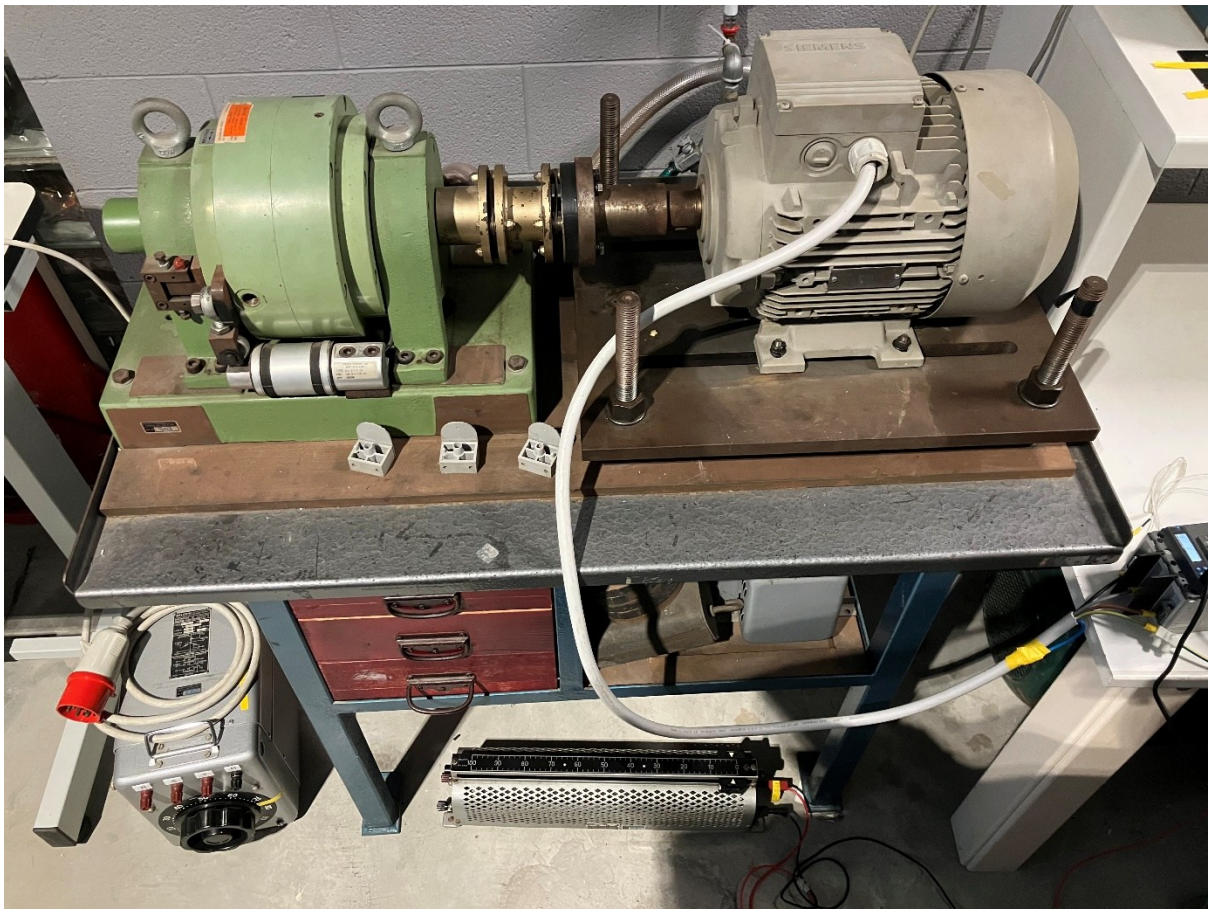

Figure 2.2: An image of the Test Bench.

Figure 2.3: Side view of the Test Bench.

2.3 Braking System

A precise and dynamically adjustable braking system is essential for studying fault signatures under varying load conditions, which directly influence motor slip and fault harmonic amplitudes. The bench employs a magnetic powder brake system, offering smooth, controllable torque without the need for a secondary generating machine, that though could offer regenerative energy back to the grid, but can be complex to control and can inject harmonics that make the measurements more difficult.

2.3.1 Magnetic Powder Brake: VIBRO-METER Model 1 PB 115

A VIBRO-METER Model 1 PB 115 magnetic powder brake is shown in Figure x below. This device provides the precise, adjustable, and stable braking torque essential for simulating various load conditions on the motor under test. Unlike systems that use a secondary machine in generator mode, a magnetic powder brake offers direct, rapid, and smooth torque control through an electromagnetic principle, making it ideal for steady-state diagnostic testing.

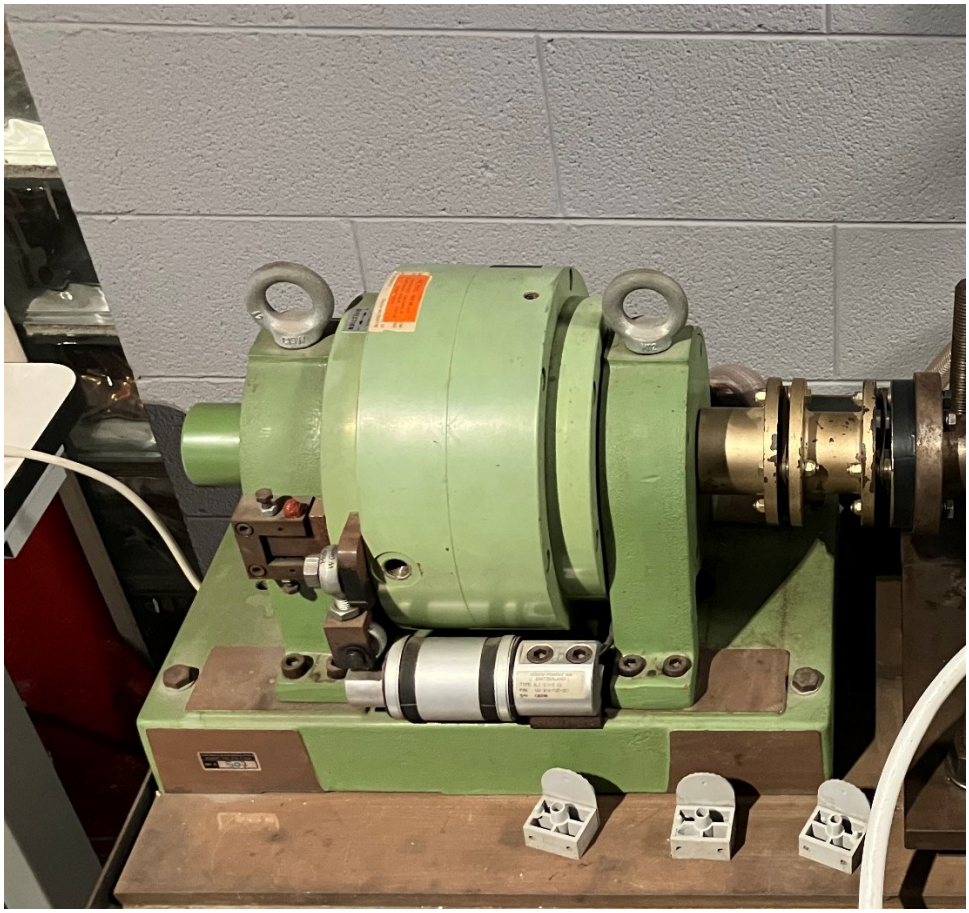

Figure 2.4: An image of the Magnetic Powder Brake on the test bench.

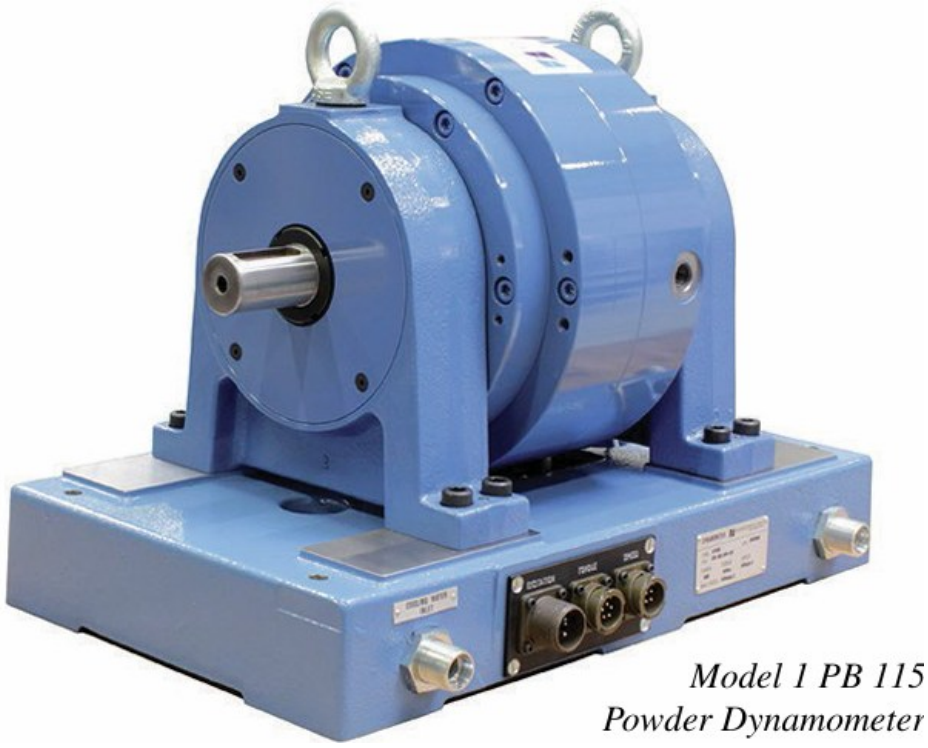

Figure 2.5: An image of the Powder Dynamometer from the manual [7].

Operating Principle:

The brake consists of a stationary stator, which houses an excitation coil, and a rotating drum rotor. The rotor is a cylinder featuring grooved toothed rings. The critical component is the air gap between the stator and rotor, which is filled with fine magnetic powder (e.g., iron filings). When the excitation coil is de-energized, centrifugal force distributes the powder within the gap. Upon applying a direct current to the coil, a magnetic field is generated. This field causes the magnetic particles to align into chains or columns that bridge the gap between the stator and the rotating grooves, creating a shear resistance due to friction. The resulting braking torque is directly and linearly proportional to the excitation current, allowing for precise control from zero to the maximum rated torque. A small residual torque (declared to be 2 Nm) persists even when de-energized, due to remnant powder in the gap.

Performance Characteristics and Operational Limits:

The performance of the Model 1 PB 115 is defined by its torque-speed and power-speed characteristics, as provided by the manufacturer and shown in Figure x (along with the similar model 2 PB 115). Key operational insights are derived from these curves:

Constant Torque Region: From standstill and up to approximately 480 rpm, the brake can deliver a near-constant maximum torque of 100 Nm (at full excitation current of 2.5 A). Within this range, the dissipated mechanical power increases linearly with speed.

The following figure shows the Torque-Speed-Power Characteristics of a series Powder Dynamometer.

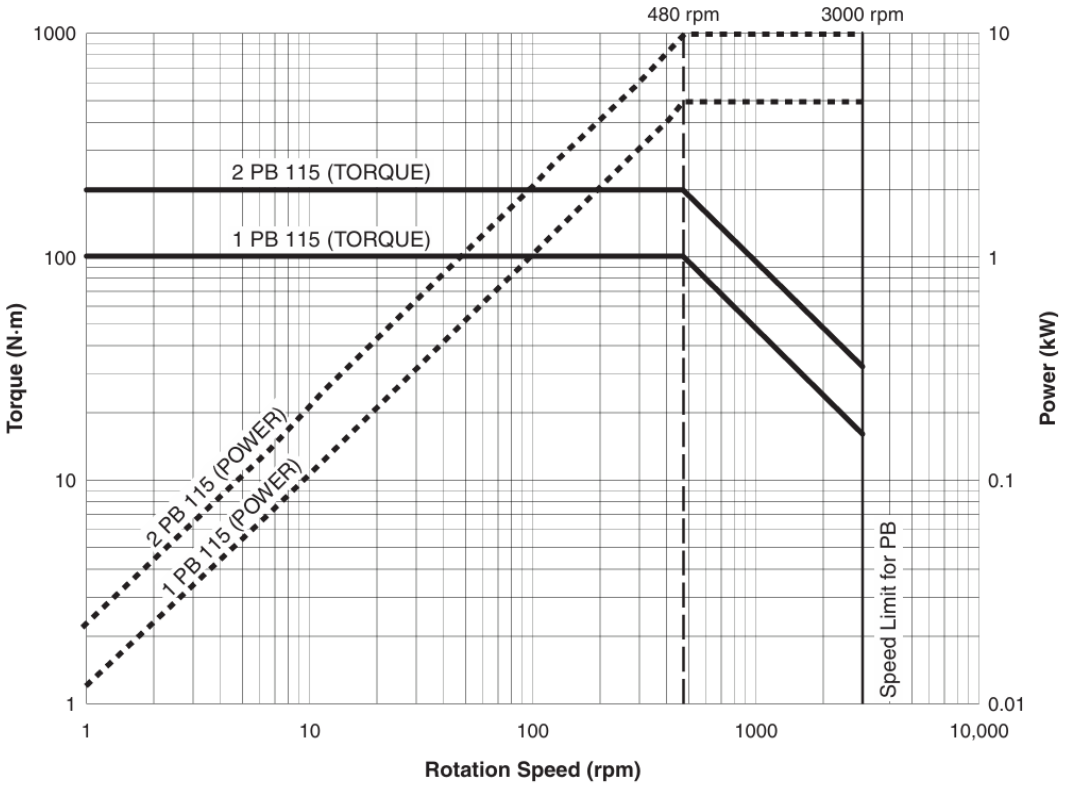

Figure 2.6: Torque-Speed-Power Characteristics of a series Powder Dynamometer [7].

Constant Power Region: Beyond 480 rpm, the maximum sustainable torque decreases inversely with speed to maintain a constant maximum dissipated power of 5 kW. This is due to thermal limits in dissipating the heat generated by friction. Note that this region has a linear decreasing torque in the previous figure (Figure 2.6) because the figure has a double logarithmic (log-log) scale. Otherwise, the torque trace is a hyperbole in the constant power region(as for electric motors in flux-weaking region).

Maximum Speed: The brake has an absolute maximum speed limit of 3000 rpm, beyond which operation is not safe or effective.

For this experimental study, given the motor's rated speed of 1455 rpm, the brake operates primarily in its constant power region. At this speed, the maximum applicable braking torque is approximately 32 Nm, which is slightly less than the motor's rated torque of 36.1Nm (motor has 5.5 kW and 1455 rpm rated power and speed). Though slightly overloading the brake at full motor power, this system ensures that the motor can be loaded across its full operational range without exceeding the brake's thermal capacity (at least for short tests, as carried out in the work).

Cooling System: The conversion of mechanical energy into heat necessitates an efficient cooling system. The Model 1 PB 115 employs a forced water-cooling circuit. An open-loop system was implemented for the test bench, where tap water is circulated through internal channels in the brake housing and then drained. This simple and cost-effective solution is adequate for the intermittent duty cycle of laboratory testing. The brake is also equipped with a thermal safety switch that disables the excitation circuit in the event of overheating, protecting the unit from damage.

Integration and Specification Summary:

The brake is connected to the motor shaft via an elastic coupling, which absorbs torsional vibrations and compensates for minor misalignments. Its rapid torque response and excellent stability make it ideal for maintaining steady-state load points required for clear MCSA spectral analysis. The key specifications of the brake are summarized in Table 2.2 below.

Table 2.2: Technical Specifications of the VIBRO-METER 1 PB 115 Brake.

Parameter	Specification
Model	1 PB 115
Residual Torque	~2 Nm
Maximum Torque	100 Nm
Nominal Braking Power	5 kW
Nominal Speed	480 rpm
Maximum Speed	3000 rpm
Excitation Current	2.5A
Nominal Excitation Voltage	30 V DC
Cooling	Water, open loop
Water Consumption	~30 l/kWh (for $\Delta T=30°C$)

2.3.2 DCU Control Unit

The Digital Control Unit (DCU) is an electronic controller and power supply that governs the operation of the magnetic powder brake. It receives a torque setpoint (either from its front panel or a remote analog input) and uses a closed-loop control algorithm to adjust the current supplied to the brake coil, maintaining the desired torque output regardless of speed variations. Note that this control unit can also be used with other brake units of the same brand i.e. the eddy current brakes, which have a torque curve strongly dependent on speed (considering a given constant excitation current).

2.3.3 DUD Display Unit

The Digital Display Unit (DUD) serves as the primary human-machine interface for the braking system. It is integrated with the DCU and provides real-time digital readouts of key parameters, including:

- Applied Braking Torque (in Nm)
- Rotational Speed (in RPM)
- Excitation Current (in A)
- System status and alarms

Unfortunately, the display of this unit is not working due to a failure happened in previous works; however, the data can be extracted and read by an oscilloscope through analogue output ports.

The DCU and DUD are shown in the following image.

Figure 2.7: DUD and DCU of the test bench.

2.3.4 Elastic Coupling for Brake-Motor Connection

A flexible, elastomeric coupling is used to connect the motor shaft to the brake input shaft. This coupling serves two critical purposes: it compensates for minor misalignments between the motor and brake, and it dampens torsional vibrations and transient torque spikes, protecting the integrated sensors and ensuring a smooth transmission of torque.

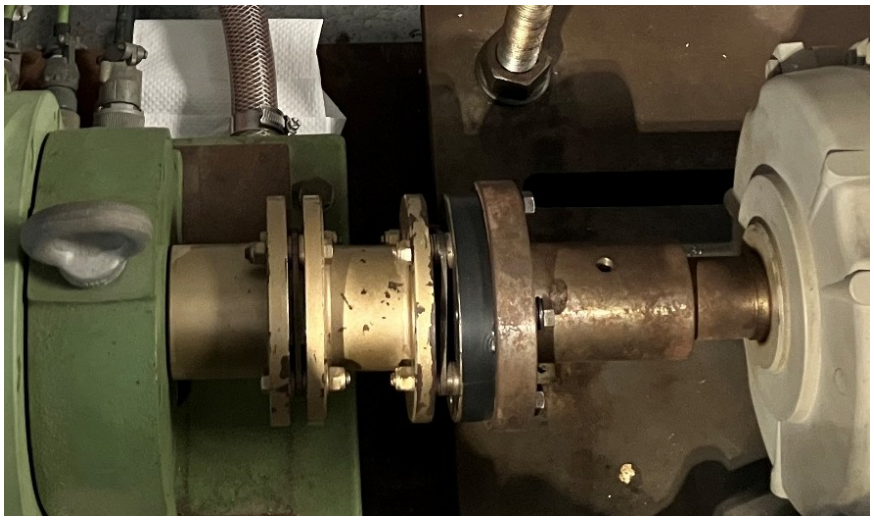

Figure 2.8: An image of the coupling between Motor and Brake.

2.3.5 Torque and Speed Sensors

The braking system is equipped with high-precision, factory-calibrated sensors mounted to provide direct measurement of mechanical variables:

Reaction Torque Sensor: This sensor measures the reaction torque transmitted from the brake to its grounding support. Due to the reaction law, this torque is equal (and opposed) to the torque transmitted from the motor to the load.

Though the bandwidth of this sensor is not comparable with in-line shaft torque sensors, it provides precise load measurement, which is essential for validating the load-dependent behaviour of MCSA fault signatures (e.g., the increase of sideband amplitude with slip).

A zoomed image of the sensor is depicted in the following.

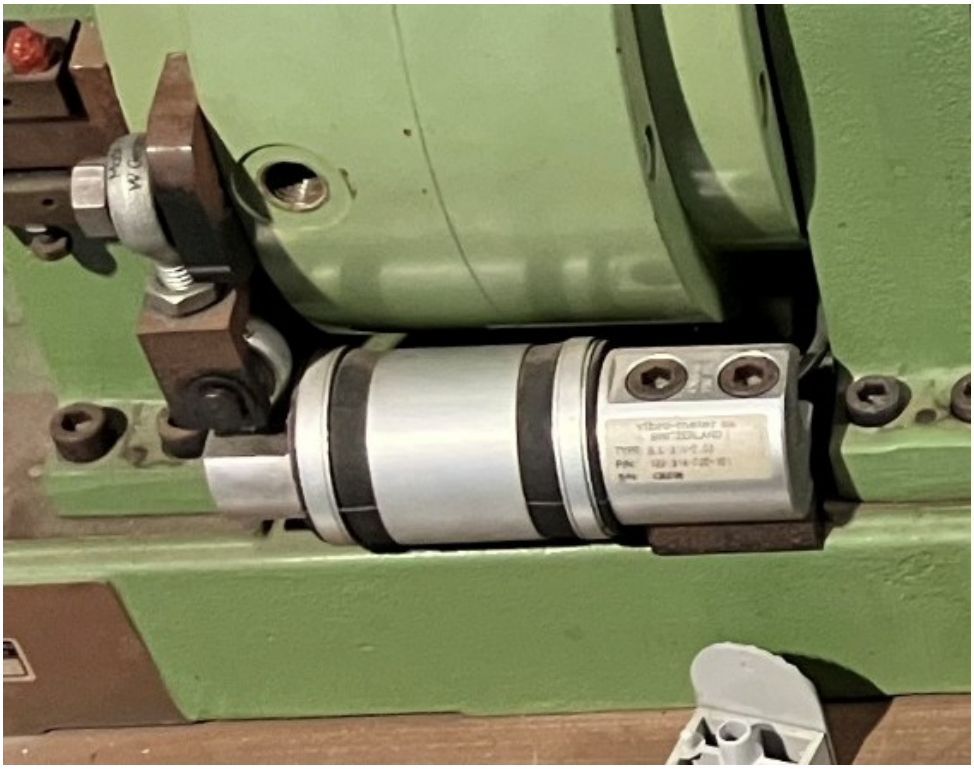

Figure 2.9: An image of the Torque Sensor.

Digital Optical Speed Sensor: A non-contact optical encoder is connected to the non-drive end shaft of the brake. It provides a high-resolution pulse train for the accurate, real-time measurement of rotational speed (RPM). The pulsed signal is conditioned through circuitry inside the DCU and DUD and is outputted in analogue form. The measured speed is used to calculate the precise motor slip (s), a critical parameter in determining the theoretical frequency location of fault-related sidebands.

2.4 ABB Ekip Connect Trip Unit

To ensure robust electrical protection and to integrate an industrial-grade source of validation data, the test bench incorporates an ABB SACE Tmax XT moulded-case circuit breaker, equipped with an advanced Ekip Connect electronic trip unit and monitoring system. This component serves a dual critical role, as a fundamental safety device protecting the motor and downstream equipment from electrical faults, and as a precise digital measurement node that enriches the experimental dataset. A picture of the apparatus is depicted in the following.

Figure 2.10: An image of the ABB SACE Tmax.

2.4.1 Device Selection and Integration

The selection of this specific breaker family was driven by the need to combine laboratory-grade measurement accuracy with the ruggedness and reliability required for continuous operation under variable load and fault conditions. The integrated Ekip Connect electronic trip unit transforms a standard protective device into an intelligent sensor. It provides comprehensive, three-phase electrical measurements that are timestamped and communicated digitally, creating a perfect complement to the transient-focused data from the primary DAQ system. Its native support for the Modbus TCP/IP protocol allowed for seamless integration into the test bench's data network, enabling synchronous logging of electrical parameters alongside vibrational and high-speed current data.

2.4.2 Technical Specifications and Compliance

The SACE Tmax XT breaker is engineered for industrial environments, ensuring its performance and safety within the laboratory setting. It is fully compliant with the IEC/EN 60947-2 standard for low-voltage circuit breakers, as well as relevant CE directives for Low Voltage (LVD) and Electromagnetic Compatibility (EMC). Key construction features that guarantee operational safety and reliability include:

Positive Contact Indication: A mechanical lever provides clear, unambiguous status of the contacts (I=Closed, O=Open).

Full Electrical Isolation: In the open position, it provides a safe isolation distance compliant with disconnector standards.

Environmental Robustness: The device features a high IP (Ingress Protection) rating, resistance to vibration, and is tropicalized, ensuring stable operation in typical laboratory conditions.

Wide Operational Range: It functions reliably within an ambient temperature range of -25°C to +70°C without performance derating up to an altitude of 2000 meters.

2.4.3 Ekip Connect Software: Configuration, Data Acquisition, and Diagnostics

The full capabilities of the trip unit are unlocked through the dedicated Ekip T&P unit USB communication module; in fact, this module permits the connection to a PC and the use of the dedicated PC software "Ekip Connect 3". This platform served as the central hub for configuration, real-time monitoring, and data retrieval:

Configuration & Commissioning: The software's intuitive interface was used to set precise protection thresholds (e.g., long-time and instantaneous overcurrent settings) tailored to the motor's rated current, ensuring safe operation during fault-seeded tests.

Real-Time Monitoring & Data Logging: A primary function for this research was the software's ability to stream and log a comprehensive suite of electrical parameters. This includes true RMS current per phase, line-to-line voltage, active/reactive power, power factor, energy consumption, and current unbalance. All data is communicated via Modbus TCP/IP or USB and logged with precise timestamps.

Event Analysis: The software maintains detailed logs of all trips, alarms, and warnings. This diagnostic history proved invaluable for post-test analysis, allowing for the correlation of protective device events with specific experimental phases or severe fault conditions.

The next image shows the T&P Unit and a screen of the Ekip Connect 3 software.

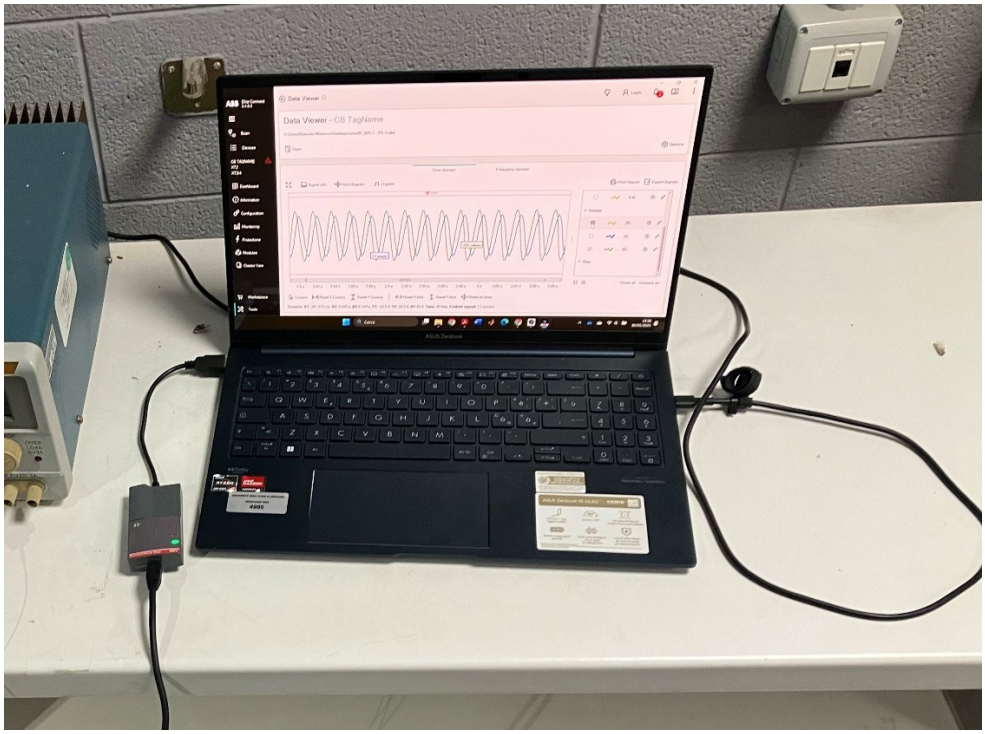

Figure 2.11: An image of a PC connected to SACE Tmax XT by an Ekip T&P unit.

2.4.4 Role in the MCSA Experimental Framework

Within the context of Motor Current Signature Analysis, this system is not merely protective against “instantaneous” faults, but it can be implemented to carry out motor diagnostics. It can be used in two ways to provide two layers of critical value:

Validation of Electrical Baseline: The highly accurate RMS current and power measurements serve as an authoritative reference to validate the signals from the primary Hall-effect current transducer and voltage sensors. The electrical variables on each phase of the motor can be analysed to see if the system is symmetric, as expected in a three-phase motor. Moreover, having voltage measures, if the current absorbed is not balanced, it can be understood if it is because of the voltage-supply unbalance or motor asymmetry. This validation ensures the integrity of the foundational data used later for spectral analysis.

Signal signatures: Since the breaker permits data acquisition at enough high sampling frequency and has an acceptable memory to save an adequate time sequence, frequency-domain analysis can be carried out on voltage and current signals. With this kind of data, MCSA can be carried out localizing some fault in the motor that can be of destructive effect many months later than when they are detected (e.g. in the case of broken rotor bar faults).

2.5 Rheostat and simulated voltage unbalances

To comprehensively study the effects of supply asymmetry on motor performance and fault signatures, the test bench incorporates a rheostat system. This setup allows for the precise and controlled introduction of voltage unbalances, a common power quality issue in industrial

environments known to exacerbate motor faults such as stator winding failures and broken rotor bars. Below some pictures of the rheostat are shown:

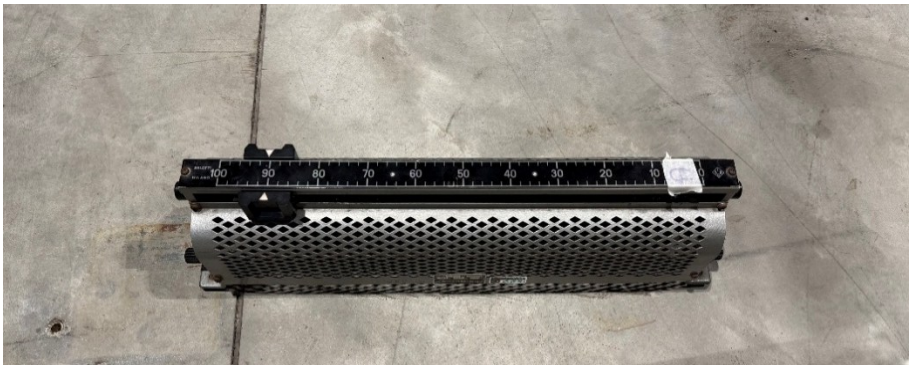

Figure 2.12: The Rheostat used in the tests.

Figure 2.12: A closeup of the rheostat parameter plate.

As shown in Figure 2.12, the main values of the rheostat are a maximum resistance of 4.89 Ω and a rated current of 10 A. Note that the motor in star connection has a rated current of 11.4 A. However, since the motor has not been loaded at its full load for long time sessions, the rheostat fitted well into the experiment.

Purpose:

A balanced three-phase supply is fundamental to the optimal operation of induction motors. Voltage unbalance causes negative sequence currents, leading to increased losses, overheating, and torque pulsations. By artificially creating defined unbalance conditions, the experimental framework can isolate and analyse their specific impact on Motor Current Signature Analysis (MCSA) indicators and validate the robustness of diagnostic algorithms under non-ideal supply conditions.

The unbalance simulation is achieved using an adjustable rheostat connected in series with one phase of the motor supply, upstream of the ABB circuit breaker. Note that with this connection the circuit braker is able to see directly the voltage unbalance.

Below is an image of the configuration in which rheostat is connected in the test bench.

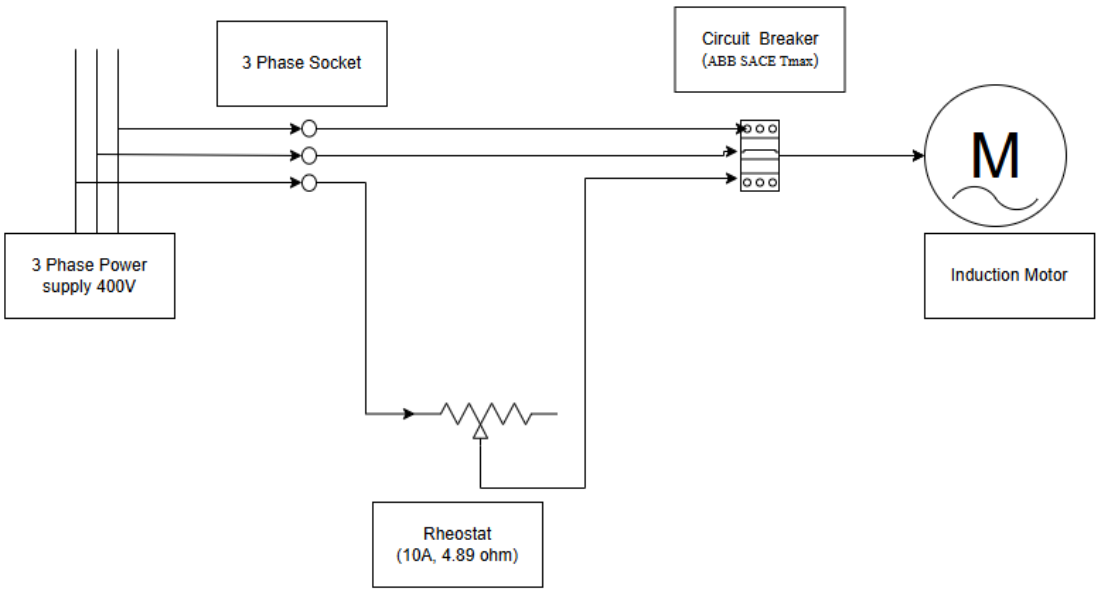

Figure 2.13: Test bench electric supply scheme.

Chapter 3 – Signal Processing and Power Quality Analysis Using MATLAB

3.1 Introduction

This chapter presents the methodology used to analyse the measured electrical signals through MATLAB. The purpose of this analysis is to evaluate the behaviour and quality of a three-phase electrical system by examining time-domain waveforms, voltage and current unbalance, harmonic content (frequency domain analysis), phase relationships, and total harmonic distortion (THD).

The experimental data were imported into MATLAB as a matrix containing time samples, three phase currents, and three-line voltages. A structured signal processing procedure was then implemented to extract useful electrical parameters from the measurements.

The analysis performed in this chapter consists of the following main stages:

1. Separation of the imported data matrix into individual signals.
2. Time-domain visualization of currents and voltages.
3. Calculation of voltage and current unbalance according to the NEMA definition.
4. Frequency-domain analysis using the Fast Fourier Transform (FFT).
5. Extraction of the fundamental phase angle of the fundamental harmonic (50 Hz).
6. Comparison of current and voltage spectra.
7. Calculation of total harmonic distortion (THD).

These steps allow a complete characterization of the electrical signals both in the time domain and the frequency domain.

It must be said here that differently from the previous thesis based on the ABB Circuit breaker acquisitions [11], in this thesis a sampling frequency of 2400 Hz is chosen (instead of 4800 Hz). Given a fixed device buffer memory, with lower sampling frequency longer time-sequences can be stored. In this case the sequences are long about 6.83 seconds. Table 3.1 summarizes the corresponding acquisition times and the resulting frequency resolution of the FFT.

Table 3.1: Sampling frequencies and corresponding acquisition times (and frequency resolutions) settable in the Ekip M Touch LRIU.

Sampling frequency [Hz]	Acquisition time [s]	Frequency resolution in spectra [Hz]
2400	6.8	0.147
4800	3.4	0.294
9600	1.7	0.588

The frequency resolution Δf of the Fast Fourier Transform is directly related to the acquisition time T by the expression:

$$\Delta f = \frac{1}{T}$$

For a given sampling frequency F_s and number of samples N, the relation is $\Delta f = F_s/N$. A longer acquisition time therefore yields a finer frequency resolution, which is beneficial for accurately distinguishing closely spaced harmonic components.

3.2 Data Import and Signal Separation

The measured data were imported into MATLAB as a matrix. Each column of the matrix represents a different measured quantity. The rows in a column represent the sequence of the samples of the considered quantity. The columns were separated into individual variables to simplify further processing. Below is represented the code (used in one of the seven acquired cases) used to separate the matrix columns imported in MATLAB and store them into column vectors with representative names.

```
1  timex1 = e2(:,1);
2  curr1  = e2(:,2);
3  curr2  = e2(:,3);
4  curr3  = e2(:,4);
5  volt12 = e2(:,5);
6  volt23 = e2(:,6);
7  volt31 = e2(:,7);
```

Figure 3.1: Picture of MATLAB code used to separate the matrix columns imported.

The structure of the matrix is defined as follows:

- Column 1: Time vector (s)
- Column 2: Phase current I_1 (A)
- Column 3: Phase current I_2 (A)
- Column 4: Phase current I_3 (A)
- Column 5: Line voltage V_{12} (V)
- Column 6: Line voltage V_{23} (V)
- Column 7: Line voltage V_{31} (V)

Below is a picture of the matrix from the import-data window of one of the cases.

	A	B	C	D	E	F	G
	Var1	Var2	Var3	Var4	Var5	Var6	Var7
	Number	Number	Number	Number	Number	Number	Number
1	t	IL1	IL2	IL3	V12	V23	V31
2	0	-16.5569	20.8626	-4.245	446.902	-482.7713	35.8235
3	0.000417	-15.6385	21.4269	-5.7324	410.1634	-506.2876	96.0784
4	0.000833	-14.6451	21.8003	-7.1041	361.3464	-520.5164	159.0784
5	0.00125	-13.4444	21.7084	-8.2039	298.7124	-517.634	218.8758
6	0.001667	-12.1348	21.0762	-8.8716	231.7778	-505.3726	273.549
7	0.002083	-10.7331	19.9469	-9.1484	160.268	-486.2026	325.8889
8	0.0025	-9.1314	18.4064	-9.2144	82.9477	-461.3137	378.2745
9	0.002917	-7.3826	16.6133	-9.1657	4.2092	-427.7778	423.5229
10	0.003333	-5.6107	14.6961	-9.0202	-69.5425	-391.085	460.5817
11	0.00375	-3.7686	12.7242	-8.9044	-140.4118	-355.0784	495.4445
12	0.004167	-1.7234	10.6579	-8.8979	-211.2353	-304.2941	515.4837

Figure 3.2: Picture of the matrix from the import-data window of one of the cases.

As said, after importing the matrix, each column was assigned to a separate MATLAB variable. This step allows independent manipulation of the time signal, currents, and voltages during the subsequent analysis.

3.3 Time-Domain Analysis of Electrical Signals

The first step in the analysis consists of observing the raw signals in the time domain. Plotting the signals as a function of time provides an initial understanding of waveform shape, amplitude, and symmetry between phases. In the following figures we have the codes used to obtain the plots.

```
8
9   figure
10  plot(timex1, curr1, timex1, curr2,  timex1, curr3, linewidth=2);
11  xlabel('Time, (s)')
12  ylabel('Phase current (A)')
13  title('Raw Signals: current')
14  legend('Current I1 [A]','Current I2 [A]','Current I3 [A]')
15  grid
    xlim([0 0.3])
```

Figure 3.3: Code used to plot time domain currents.

```
figure
plot(timex1, volt12, timex1, volt23,  timex1, volt31, linewidth=2);
xlabel('Time, (s)')
ylabel('Phase voltages (V)')
title('Raw Signals: voltages')
legend('Voltage V12 [V]','Voltage V23 [V]','Voltage V31 [V]')
grid
xlim([0 0.3])
```

Figure 3.4: Code used to plot time domain voltages.

Two different plots were generated:

1. Three-phase currents versus time.
2. Three-line voltages versus time.

Below are two examples of the plots.

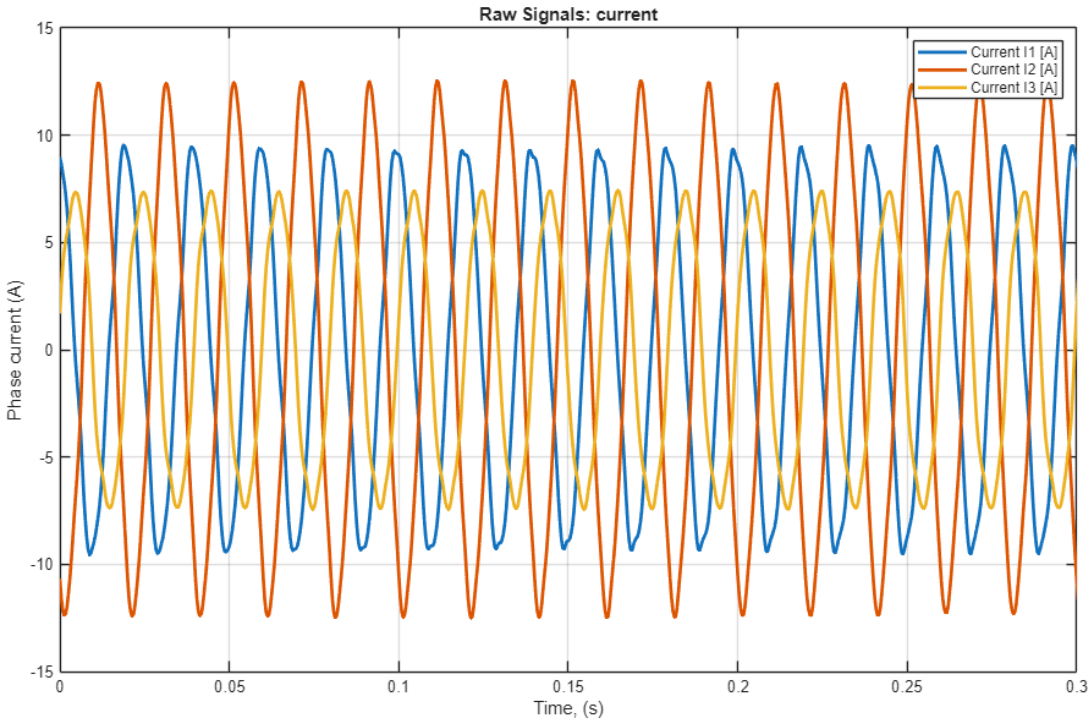

Figure 3.5: Three-phase currents versus time (unbalanced case).

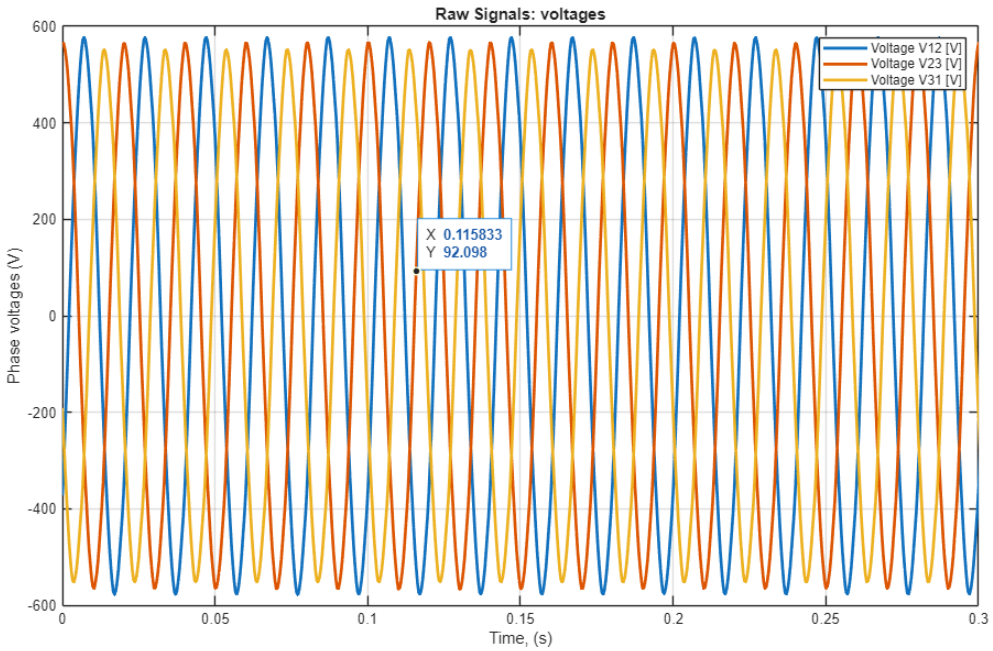

Figure 3.6: Three-phase voltages versus time (unbalanced case).

The time interval displayed in the plots was limited to 0–0.3 seconds to clearly visualize several cycles of the 50 Hz fundamental frequency.

The current plot allows verification of:

- amplitude similarity between phases.
- waveform shape.
- possible distortions.

Similarly, the voltage plot provides insight into:

- the magnitude balance between the three-line voltages.
- waveform quality
- possible disturbances in the supply.

These plots serve as the initial qualitative assessment of the electrical system before performing numerical analysis.

3.4 Voltage and Current Unbalance Calculation

After the time-domain inspection, the degree of unbalance in the three-phase system was quantified. Unbalance occurs when the magnitudes of the three phase quantities are not equal.

The voltage and current unbalance were calculated using the definition provided by the National Electrical Manufacturers Association (NEMA) publication no. MG 1-1993. According to this method, the unbalance percentage is defined as [8], [9]:

$$Current\ Unbalance\ (\%) = 100 * \frac{Maximum\ \ Current\ Deviation\ from\ Average}{Average\ Current}$$

$$Voltage\ Unbalance\ (\%) = 100 * \frac{Maximum\ \ Voltage\ Deviation\ from\ Average}{Average\ Voltage}$$

Note, that the average of the voltage must be done with line-voltages. In fact, using these voltages in the unbalance factor calculation, the phase angle unbalance is included [9]. It is important to note that the NEMA definition of voltage unbalance differs from the "true" definition used in power systems engineering, which is based on symmetrical components [10].

The true definition expresses voltage unbalance as the ratio of negative sequence voltage to positive sequence voltage:

$$\%\text{VUF} = \frac{V_2}{V_1} \times 100$$

where V_1 and V_2 are the positive and negative sequence voltages, respectively [9]. Pillay et al. [10] demonstrated that for a given NEMA unbalance percentage, there exists a range of true unbalance values. For example, a 5% unbalance using the NEMA definition corresponds to a true unbalance ranging from 5% to 5.8%, depending on the nature of the voltage deviation. However, their analysis concluded that this difference is not significant for motor derating purposes up to 5% unbalance, as the resulting loss increase is only approximately 1% [10].

To obtain the results, firstly, the root mean square (RMS) values of the three phase voltages and currents were calculated from the time domain instantaneous data. The RMS value represents the effective magnitude of an alternating signal.

The maximum deviation of any voltage from the average value was then determined. The voltage unbalance percentage was computed using the formula described above.

The same procedure was applied to the three currents (I_1), (I_2), and (I_3). The resulting values provide a quantitative measure of how balanced the three-phase system is.

The following figures show the MATLAB codes used to calculate the unbalances.

```
% Voltage Unbalance
Vrms12 = rms(volt12);
Vrms23 = rms(volt23);
Vrms31 = rms(volt31);

V = [Vrms12 Vrms23 Vrms31];

Vavg = mean(V);
Vmax_dev = max(abs(V - Vavg));

V_unbalance_percent = 100 * (Vmax_dev / Vavg);

fprintf('Voltage Unbalance (NEMA) = %.3f %%\n', V_unbalance_percent);
```

Figure 3.7: MATLAB code used to calculate Voltage Unbalance.

```
% Current Unbalnce
Irms1 = rms(curr1);
Irms2 = rms(curr2);
Irms3 = rms(curr3);

I = [Irms1 Irms2 Irms3];

Iavg = mean(I);
Imax_dev = max(abs(I - Iavg));

I_unbalance_percent = 100 * (Imax_dev / Iavg);

fprintf('Current Unbalance (NEMA) = %.3f %%\n', I_unbalance_percent);
```

Figure 3.8: MATLAB code used to calculate Current Unbalance.

Note that according to [9], there are several possible voltage unbalance conditions including: single-phase under-voltage unbalance, two-phase under-voltage unbalance, single-phase over-voltage unbalance, unequal single-phase angle displacement, etc.

Below is the table (3.2) of the voltage and current unbalance calculated in the laboratory where,

- a is the case for 80% load and 90%R unbalance,
- b is the case for 80% load and 50%R unbalance,
- c is the case for 80% load and 0%R unbalance,
- d is the case for 30% load and 90%R unbalance,
- e is the case for 30% load and 50%R unbalance,
- f is the case for 30% load and 0%R unbalance,
- g is the case for 0% load and 0% R unbalance,

Note that the percentage of unbalance %R is referred at the percentage of rheostat resistor inserted during the tests. . So, given a total rheostat resistance of 4.89 Ω, 90%R corresponds to 4.4 Ω and 50%R to 2.44 Ω.

Table 3.2: Voltage and Current Unbalances in percentage.

Cases	Voltage Unbalance in Percentage	Current Unbalance in percentage
a	6.50	37.87
b	4.23	25.07
c	0.23	2.47
d	3.73	34.57
e	2.54	24.79
f	0.21	2.82
g	0.09	1.9

The substantial difference between voltage unbalance and current unbalance observed in Table 3.2 is consistent with the findings of von Jouanne and Banerjee [9], who noted that "a small unbalance in the phase voltages can cause a disproportionately larger unbalance in the phase currents." This amplification occurs because the negative sequence impedance of induction motors is relatively low, allowing even modest voltage unbalances to drive significant negative sequence currents [9], [10]. In the most severe case (case a), a 6.50% voltage unbalance produced a 37.87% current unbalance, representing an amplification factor of approximately 5.8, which aligns with the range of 6 to 10 times reported in the literature [9].These indicators are important in power systems because excessive unbalance can lead to overheating, efficiency reduction, and mechanical stress in electrical machines.

3.5 Frequency-Domain Analysis Using FFT

While time-domain analysis shows waveform behaviour, it does not clearly reveal harmonic components. Therefore, frequency-domain analysis was performed using the Fast Fourier Transform (FFT).

The FFT converts a time-domain signal into its frequency spectrum, showing the magnitude of each frequency component present in the signal.

3.5.1 Sampling Frequency

The sampling frequency was determined from the time vector using:

$$F_s = \frac{1}{t_2 - t_1}$$

where t_1 and t_2 are two consecutive time samples. This parameter is required for accurate frequency scaling in the FFT results.

The sampling frequency F_s is a critical parameter for frequency-domain analysis as it determines the Nyquist frequency ($F_{Nyquist} = F_s/2$), which defines the maximum frequency that can be accurately represented in the spectrum. Additionally, the frequency resolution of

the FFT is given by $\Delta f = F_s/N$, where N is the number of samples. For the measurements in this study, the consistent sampling frequency ensures reliable harmonic analysis up to the frequencies of interest.

This parameter is required for accurate frequency scaling in the FFT results.

Below is the figure of the code used.

```
52    %% Sampling parameters
53    Fs = 1/(timex1(2) - timex1(1));
54    L  = length(timex1);
55
```

Figure 3.9: MATLAB code used for Sampling Frequency.

3.5.2 DC Component Removal

Before performing the FFT, the mean value of each signal was removed. This step eliminates the DC component and ensures that the spectrum represents only the alternating components of the signal. Below is the figure for the Figure MATLAB code used for DC component removal.

```
56    %% Remove DC component
57    curr1 = curr1 - mean(curr1);
58    curr2 = curr2 - mean(curr2);
59    curr3 = curr3 - mean(curr3);
60
```

Figure 3.10: MATLAB code used for DC component removal.

3.5.3 Windowing

A Hann window was applied to the signals before computing the FFT. Windowing reduces spectral leakage, which occurs when the analysed signal does not contain an integer number of periods within the observation window.

The Hann window improves the accuracy of the harmonic magnitude estimation.

Below is the figure for the MATLAB code used for applying Hann window.

```
%% Apply Hann window
w = hann(L);

curr1w = curr1 .* w;
curr2w = curr2 .* w;
curr3w = curr3 .* w;

```

Figure 3.11: MATLAB code used for applying Hann window.

3.5.4 Single-Sided Spectrum

After computing the FFT, the double-sided spectrum was converted into a single-sided spectrum. This representation contains only the positive frequencies and doubles the amplitude of the non-DC components. The frequency axis was then generated to represent the correct frequency values corresponding to each FFT bin.

For visualization purposes, the spectra were plotted only up to 200 Hz. This range includes the fundamental component at 50 Hz and the most relevant lower-order harmonics.

Below is the figure of the code used for FFT calculations.

```
%% Frequency axis
f = Fs*(0:(L/2))/L;

%% -------- FFT Phase 1 --------
Y1 = fft(curr1w);
P2_1 = abs(Y1/L);
P1_1 = P2_1(1:L/2+1);
P1_1(2:end-1) = 2*P1_1(2:end-1);

%% -------- FFT Phase 2 --------
Y2 = fft(curr2w);
P2_2 = abs(Y2/L);
P1_2 = P2_2(1:L/2+1);
P1_2(2:end-1) = 2*P1_2(2:end-1);

%% -------- FFT Phase 3 --------
Y3 = fft(curr3w);
P2_3 = abs(Y3/L);
P1_3 = P2_3(1:L/2+1);
P1_3(2:end-1) = 2*P1_3(2:end-1);

```

Figure 3.12: MATLAB code used for calculation of the FFT spectrum.

3.5.5 Normalized Spectrum and dB Representation

Two types of spectra were analysed:

- The original FFT magnitude spectrum
- The normalized spectrum

To analyse the harmonic content of the measured signals, the FFT spectra were normalized with respect to the magnitude of the fundamental frequency component (50 Hz). In this representation, the amplitude of each harmonic component is expressed relative to the fundamental harmonic.

This normalization allows the harmonic magnitudes to be compared independently of the absolute signal amplitude and highlights the relative contribution of higher-order harmonics. Such a representation is particularly useful in power quality analysis, where the interest lies in evaluating the harmonic distortion of currents and voltages and determining how significant each harmonic component is with respect to the fundamental frequency.

Furthermore, the normalized spectra facilitate the interpretation of harmonic levels and support the calculation and validation of Total Harmonic Distortion (THD), which is defined based on the ratio between the harmonic components and the fundamental component.

The normalized spectrum was obtained by dividing the spectrum by its maximum value. This operation sets the largest component to 1, making it easier to compare harmonic amplitudes relative to the fundamental component. To improve readability, the spectra were also converted to decibels (dB) using the logarithmic expression:

$$\text{Magnitude}_{\text{dB}} = 20\log_{10}(\text{Magnitude})$$

When implementing this conversion in MATLAB, a small constant [eps] is added to the magnitude before taking the logarithm. The [eps] function returns the distance from 1.0 to the next larger double-precision floating-point number (approximately 2.22×10^{-16}). Adding [eps] prevents evaluating [log10(0)] in cases where a spectral component is exactly zero, which would otherwise produce [-Inf] and cause issues when plotting or further processing the data.

The dB scale allows small harmonic components to be visualized more clearly compared to a linear scale.

Below is the figure of the code used for normalized spectrum and conversion of FFT magnitudes to dB scale.

```
%% -------- Normalize spectra (peak = 0 dB) --------
P1_1_norm = P1_1 / max(P1_1);
P1_2_norm = P1_2 / max(P1_2);
P1_3_norm = P1_3 / max(P1_3);

%% Convert FFT magnitudes to dB
P1_1_dB = 20*log10(P1_1 + eps);
P1_2_dB = 20*log10(P1_2 + eps);
P1_3_dB = 20*log10(P1_3 + eps);

%% Convert normalized spectra to dB
P1_1_dB_Norm = 20*log10(P1_1_norm + eps);
P1_2_dB_Norm = 20*log10(P1_2_norm + eps);
P1_3_dB_Norm = 20*log10(P1_3_norm + eps);

%% -------- FFT Phase 1 (dB) --------
figure;
plot(f, P1_1_dB, f, P1_1_dB_Norm)
xlim([0 200])
xlabel('Frequency (Hz)')
ylabel('Magnitude (dB)')
title('FFT of Current Phase 1 (dB)')
legend('Original','Normalized')
grid on

%% -------- FFT Phase 2 (dB) --------
figure;
plot(f, P1_2_dB, f, P1_2_dB_Norm)
xlim([0 200])
xlabel('Frequency (Hz)')
ylabel('Magnitude (dB)')
title('FFT of Current Phase 2 (dB)')
legend('Original','Normalized')
grid on

%% -------- FFT Phase 3 (dB) --------
figure;
plot(f, P1_3_dB, f, P1_3_dB_Norm)
xlim([0 200])
xlabel('Frequency (Hz)')
ylabel('Magnitude (dB)')
title('FFT of Current Phase 3 (dB)')
legend('Original','Normalized')
grid on

```

Figure 3.13: MATLAB code used for normalized spectra and conversion of FFT magnitudes to dB scale.

Below are some figures of the current and voltage normalized or non-normalized spectra:

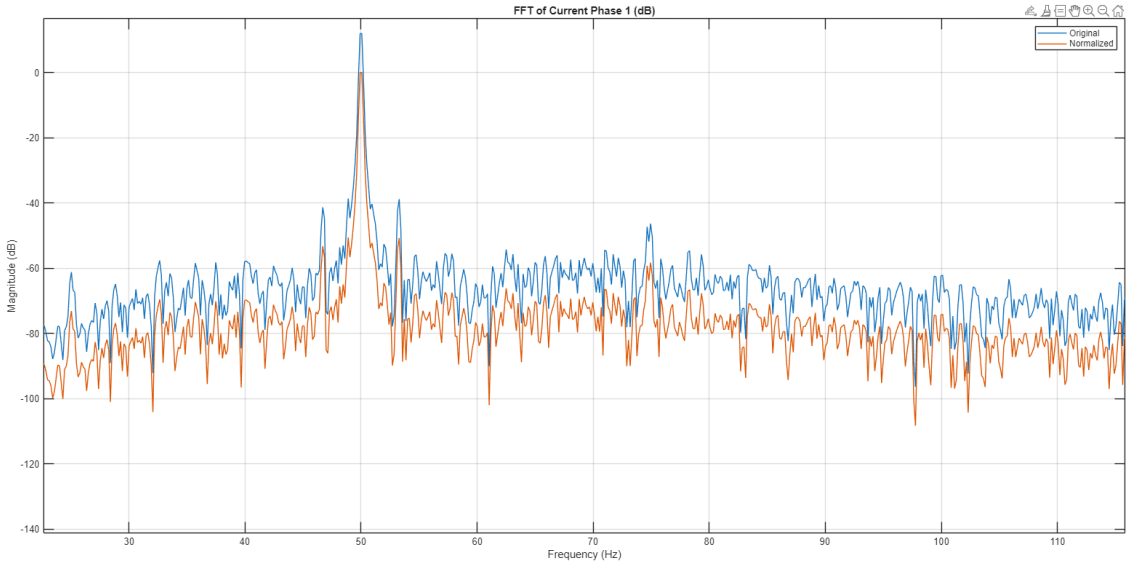

Figure 3.14: Normalized and Original Current Spectrum.

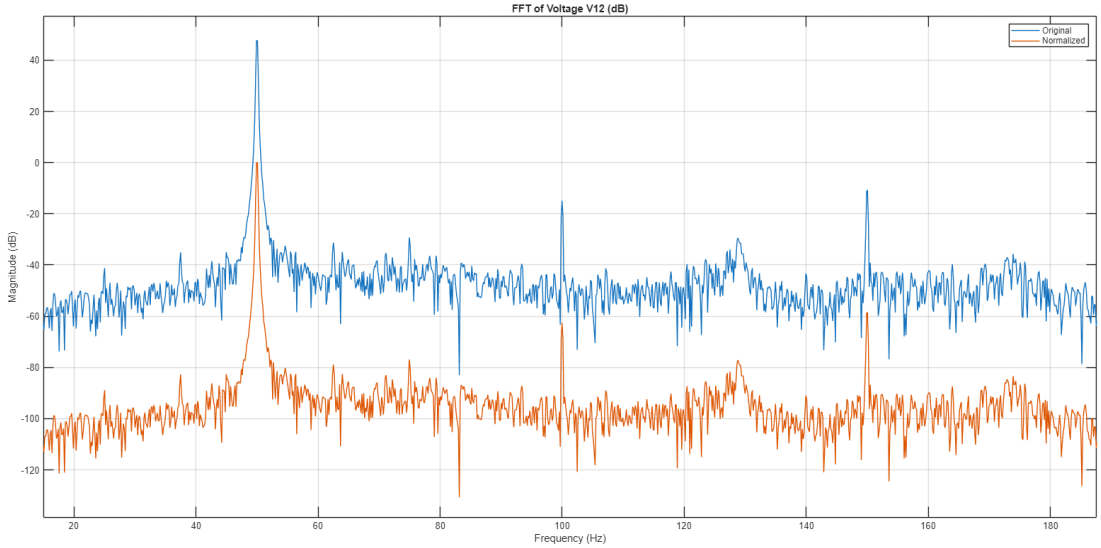

Figure 3.15: Normalized and Original Voltage Spectrum.

3.5.6 Fundamental Harmonic Phase Angle Calculation

Another important parameter extracted from the FFT is the phase angle of the fundamental frequency component. The phase angles of currents and voltages determine the power factor and reactive power flow in the system, making them essential for understanding the electrical behaviour.

The fundamental frequency of the system is 50 Hz. Therefore, the index corresponding to the frequency closest to 50 Hz was identified in the FFT frequency vector. The phase angle of each

current and voltage signal at this frequency was calculated using the complex FFT result. The phase values were then converted from radians to degrees.

Finally, the phase angles were wrapped to the range of −180° to +180° to obtain a standard phase representation.

Below is the figure of the code used for fundamental phase angle calculations.

```
%% -------- Phase of Fundamental (50 Hz) --------

% Find index closest to 50 Hz
[~, idx50] = min(abs(f - 50));

% Phase calculation
phase_I1 = angle(Y1(idx50))*180/pi;
phase_I2 = angle(Y2(idx50))*180/pi;
phase_I3 = angle(Y3(idx50))*180/pi;

% Wrap angles between -180 and 180
phase_I1 = wrapTo180(phase_I1);
phase_I2 = wrapTo180(phase_I2);
phase_I3 = wrapTo180(phase_I3);

%% -------- Save results in table --------
Current = ["I1"; "I2"; "I3"];
Phase_deg = [phase_I1; phase_I2; phase_I3];

Current_Phase_Table = table(Current, Phase_deg);

disp(Current_Phase_Table)
```

Figure 3.16: MATLAB code used for calculation of fundamental phase angle.

The resulting phase values were stored in Table 3.3 for both currents and voltages. These values are useful for evaluating phase relationships between electrical quantities.

Table 3.3 Currents and voltages phase angles (º)

	$\angle I_1$	$\angle I_2$	$\angle I_3$	$\angle V_{21}$	$\angle V_{32}$	$\angle V_{13}$
a	54.75	-151.75	-20.11	-97.80	26.34	139.55
b	105.64	-111.91	15.72	-54.35	68.81	175.51
c	90.08	-147.37	-27.70	-77.41	42.72	162.49
d	105.96	-102.52	29.81	-27.31	96.17	-147.61
e	-84.40	56.72	-174.12	137.29	-100.22	17.54
f	45.51	168.33	-72.55	-104.9	15.2	134.98
g	173.24	-64.95	54.95	47.74	167.84	-72.25

Taking the phase angle of the voltage $\mathbf{V_{21}}$, i.e. putting it to 0°, and unwrapping the angles <-180° and >180°, the relative phase angles between the line voltages are clearer.

Table 3.4 Line voltages relative phase angles (°)

Case	$\angle V_{21}$	$\angle V_{32}$	$\angle V_{13}$
a	0	124.2	-122.6
b	0	123.2	-130.1
c	0	120.1	-120.1
d	0	123.5	-120.3
e	0	122.5	-119.7
f	0	120.1	-120.1
g	0	120.1	-120.0

From table 3.4, it is clear that the rheostat method introduces in addition to a magnitude unbalance, also a phase unbalance. In fact, the cases c), f) and g) -the ones without unbalance- present phase angles of V_{32} and V_{13}very close to 120° (in absolute values). The maximum phase unbalance has been found for case b), since V_{13} is more than 10° shifted from the ideal phase of -130.1°.

Doing the same calculation with the three currents, (I_1 has been taken as reference) the relative phase angles between currents are calculated and shown in table 3.5.

Table 3.5 Line current relative phase angles (°)

Case	$\angle I_1$	$\angle I_2$	$\angle I_3$
a	0	-153.5	74.9
b	0	-142.5	89.9
c	0	-122.5	117.8
d	0	-151.5	76.1
e	0	-141.1	89.7
f	0	-122.8	118.1
g	0	-121.8	118.3

It is clear from the table that much higher phase unbalance is present from the three currents. In fact, in from cases c), F) and g), that are balanced, the angles are around the ideal 120° with tolerances of about ± 3°. In the other unbalanced cases the angles can be shifted from the ideal 120° reference up to about ± 30° .

The phase angles presented in Table 3.4 reveal how different types of unbalance conditions affect the phase relationships. According to von Jouanne and Banerjee [9], the way voltages are unbalanced significantly impacts motor performance. Several unbalance conditions are possible, including single-phase under-voltage, two-phase under-voltage, single-phase over-voltage, and unequal phase angle displacement. The variation in phase angles from the ideal 120° separation observed in Table 3.3 reflects these different unbalance mechanisms [9], [10].

To visualize the phase relationships between voltages and currents, vector (phasor) diagrams were constructed from the calculated phase angles. Figure 3.17 shows a representative phasor diagram illustrating the angular relationships between the three-line voltages and the corresponding phase voltages in balanced conditions. Note that the system is in inverse sequence, i.e. considering a counterclockwise rotation of the phasors, the quantities will pass a given point with the following order: E1, E3 and E2. This is the case for the measured quantities in the tests.

Note that, as known from the theory, the line voltages are leading the phase-voltages of 30°.

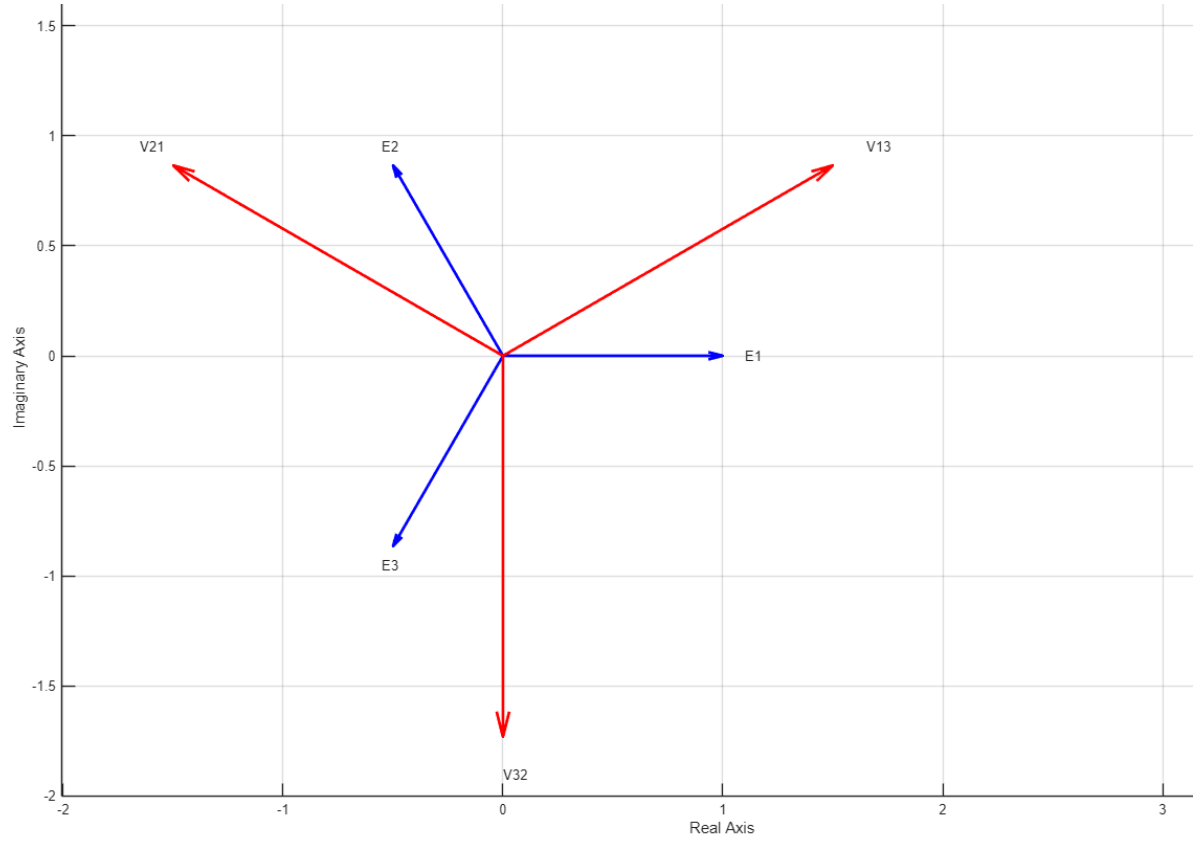

Figure 3.17: Phasor diagram showing angular relationships between line and phase voltages.

The phasor diagram reveals important information about the system's operating condition. For instance, the cosine of the phase angle φ between phase voltage and current determines the power factor:

$$\cos\ \varphi = \frac{P}{S}$$

where P is active power and S is apparent power. Note that the previous formula is valid also for unbalanced system, given P and Q as the sum of the three phases active and reactive power.

As previously mentioned, the angle φ corresponds to the phase-angle difference between correspondent phase-voltage and phase-current. In formula it is:

$$\varphi = \angle E_i - \angle I_i$$

With i=1,2,3 the number of the system phase.

In a balanced three-phase system φ is equal for all the three phases, and its cosine gives the power factor of the system.

Instead, in an unbalanced case, the power factor is an average power factor, since the φ angle will be different for every system' phase [12].

In balanced conditions, the phase angles between phases quantities (voltages or current) should be separated by approximately 120°. Deviations from this ideal indicate unbalance or distortion in the system.

Figure 3.17 presents another view of the angular calculations, including the phase current, showing the specific phase angles obtained for one of the test cases, the test **c)** that is a balanced trial. Referring to Table 3.2, in which the current and voltage angles are taken synchronously for each case, the following method is implemented to see if the phase angle calculations were correctly made.

The voltage V_{21} is found to be at -77.4°. Since the system is found to be in inverse sequence, and the load is balanced (case c)), V_{21} is leading E_2 of 30°. So, the angle of E_2 is:

$$\angle E_2 = \angle V_{21} - 30° = -77.4 - 30 = -107.4°$$

To see if the phase angle of the current is plausible, the following reasoning has been conducted:

- The induction motor is an inductive load, so the current is always lagging the phase voltage. The maximum lag possible is 90°. This represent a purely inductive load (the motor at no-load is almost in this condition). In this condition the phase angle of I_2 should be:
$$\angle I_{2\_noLoad} = \angle E_2 - 90° = -107.4 - 90 = -197.4°$$

- At the rated load the power factor is assumed to be maximum. This datum is available from the motor tag, and it is
$PF_{rated} = \cos\varphi_{rated} = 0.81$. The φ_{rated} is readily calculated with the inverse cosine function and it is: $\varphi_{rated} = \arccos(0.81) = 35.9°$. This angle represents the minimum angle between the voltage E2 and current I2. So, the angle of I2 in this condition should be:
$$\angle I_{2\_rated\_Load} = \angle E_2 - 35.9° = -107.4 - 35.9 = -143.3°$$

- The angle of I2 must be included between these two limits, and this occurred since the calculated phase of I2 is -147.4° (see table 3.2):
$$\angle I_{2\_noLoad} < -147.4 < \angle I_{2\_rated\_Load}$$

- Moreover, knowing that the load condition in test c) is approximately 80%, it is correct that the angle is closer to the $\angle I_{2\_rated\_Load}$ than to the no-load angle.

Other checks of this type are performed on the other balanced cases leading to plausible angles of current phasors.

Below is a figure of phase angle calculations of a representative test case.

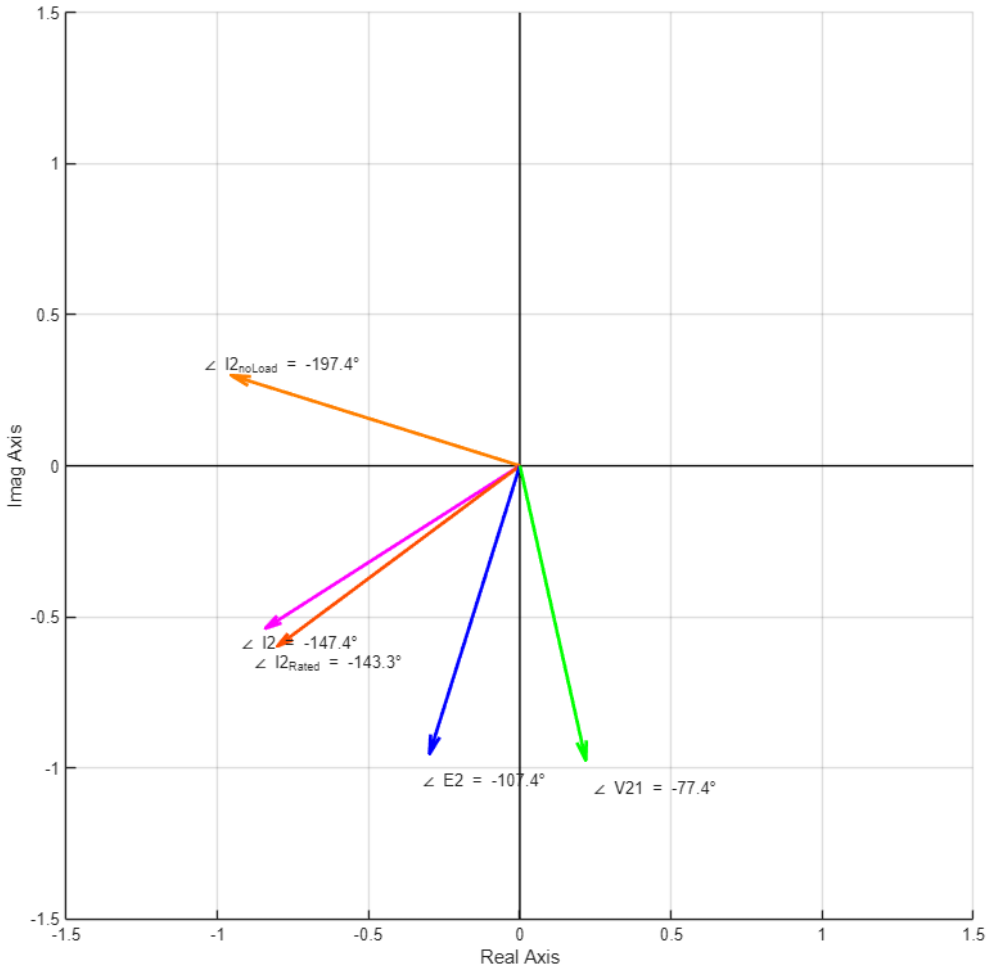

Figure 3.18: Detailed phase angle calculations for current I_2 in the test case c).

3.6 Combined Current–Voltage Spectral Comparison

To facilitate comparison between electrical quantities, the FFT spectra of the currents and their corresponding line voltages can plotted together. Below is the figure of the MATLAB code used for the plot:

```
% fft plot on same graph
%% Convert magnitudes to dB (if not already done)
P1_1_dB   = 20*log10(P1_1 + eps);   % Current phase 1
P1_2_dB   = 20*log10(P1_2 + eps);   % Current phase 2
P1_3_dB   = 20*log10(P1_3 + eps);   % Current phase 3

P1_v1_dB  = 20*log10(P1_v1 + eps);  % Voltage V12
P1_v2_dB  = 20*log10(P1_v2 + eps);  % Voltage V23
P1_v3_dB  = 20*log10(P1_v3 + eps);  % Voltage V31

%% Plot all three current-voltage pairs in one figure
figure;

% -------- Phase 1 --------
subplot(3,1,1)
plot(f, P1_1_dB, 'b', 'LineWidth', 1.5); hold on;
plot(f, P1_v1_dB, 'r', 'LineWidth', 1.5);
xlim([0 200]);
xlabel('Frequency (Hz)');
ylabel('Magnitude (dB)');
title('Phase 1: Current 1 & Voltage V12');
legend('Current 1', 'Voltage V12');
grid on;

% -------- Phase 2 --------
subplot(3,1,2)
plot(f, P1_2_dB, 'b', 'LineWidth', 1.5); hold on;
plot(f, P1_v2_dB, 'r', 'LineWidth', 1.5);
xlim([0 200]);
xlabel('Frequency (Hz)');
ylabel('Magnitude (dB)');
title('Phase 2: Current 2 & Voltage V23');
legend('Current 2', 'Voltage V23');
grid on;

% -------- Phase 3 --------
subplot(3,1,3)
plot(f, P1_3_dB, 'b', 'LineWidth', 1.5); hold on;
plot(f, P1_v3_dB, 'r', 'LineWidth', 1.5);
xlim([0 200]);
xlabel('Frequency (Hz)');
ylabel('Magnitude (dB)');
title('Phase 3: Current 3 & Voltage V31');
legend('Current 3', 'Voltage V31');
grid on;
```

Figure 3.19: MATLAB code used for Combined Current–Voltage Spectral Comparison.

Three comparisons were performed:

- Phase 1: Current (I_1) with Voltage (V_{12})
- Phase 2: Current (I_2) with Voltage (V_{23})
- Phase 3: Current (I_3) with Voltage (V_{31})

Displaying the spectra together allows observation of whether the same harmonic frequencies appear in both voltage and current signals.

Below is the figure of the combined Current-Voltage Spectra:

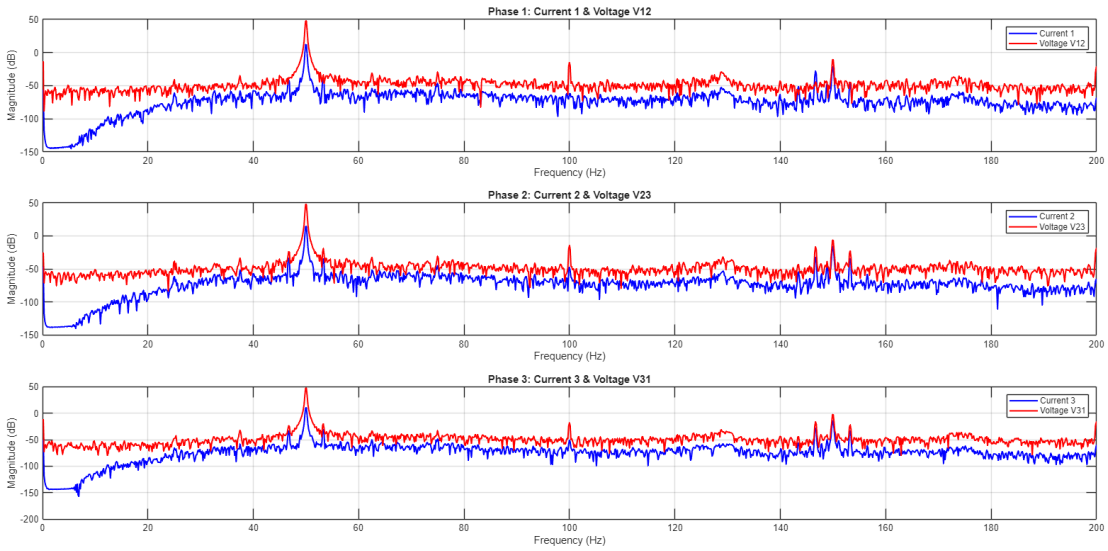

Figure 3.20: Figure of Combined Current–Voltage Spectral Comparison.

This comparison can reveal whether current harmonics originate from the supply voltage or from nonlinear loads connected to the system.

3.7 Total Harmonic Distortion (THD)

The harmonic distortion of the signals was quantified using the Total Harmonic Distortion (THD) parameter. THD measures the ratio between the energy contained in harmonic components and the energy of the fundamental component. Mathematically, THD is defined as:

$$\mathrm{THD} = \frac{\sqrt{\sum_{h=2}^{\infty} M_h^2}}{M_1} \times 100\%$$

where M_1 is the RMS magnitude of the fundamental frequency component (50 Hz), and M_h represents the RMS magnitudes of the harmonic components (at frequencies that are integer multiples of 50 Hz). The summation can include all harmonics present up to the Nyquist frequency.

In many power quality analyses, THD is also expressed in decibels relative to the carrier (dBc) using the conversion:

$$\mathrm{THD_{dBc}} = 20\log_{10}\left(\frac{\sqrt{\sum_{h=2}^{\infty} M_h^2}}{M_1}\right)$$

MATLAB's built-in thd function was used to compute THD directly from the signals. The results were obtained in decibels relative to the carrier (dBc). For better interpretation, the values were also converted into percentages using the inverse relationship:

$$\mathrm{THD_{\%}} = 100 \times 10^{\mathrm{THD_{dBc}}/20}$$

Below are the pictures of the MATLAB code used for THD calculations:

```
%% THD CALCULATION upto 20th harmonic

% Remove DC component
curr1 = curr1 - mean(curr1);
curr2 = curr2 - mean(curr2);
curr3 = curr3 - mean(curr3);

volt12 = volt12 - mean(volt12);
volt23 = volt23 - mean(volt23);
volt31 = volt31 - mean(volt31);

%%  CURRENT THD

THD1_dB = thd(curr1, Fs, 20);
THD2_dB = thd(curr2, Fs, 20);
THD3_dB = thd(curr3, Fs, 20);

% Convert dB → %
THD1 = 100 * 10^(THD1_dB/20);
THD2 = 100 * 10^(THD2_dB/20);
THD3 = 100 * 10^(THD3_dB/20);

fprintf('\n===== CURRENT THD (up to 20th harmonic) =====\n');
fprintf('THD Phase 1 = %.2f %%\n', THD1);
fprintf('THD Phase 2 = %.2f %%\n', THD2);
fprintf('THD Phase 3 = %.2f %%\n', THD3);

%% VOLTAGE THD

THD_V12_dB = thd(volt12, Fs, 20);
THD_V23_dB = thd(volt23, Fs, 20);
THD_V31_dB = thd(volt31, Fs, 20);

% Convert dB → %
THD_V12 = 100 * 10^(THD_V12_dB/20);
THD_V23 = 100 * 10^(THD_V23_dB/20);
THD_V31 = 100 * 10^(THD_V31_dB/20);

fprintf('\n===== VOLTAGE THD (up to 20th harmonic) =====\n');
fprintf('THD V12 = %.2f %%\n', THD_V12);
fprintf('THD V23 = %.2f %%\n', THD_V23);
fprintf('THD V31 = %.2f %%\n', THD_V31);
```

Figure 3.21: MATLAB code used for Current and Voltage THD calculations up to 20th harmonics.

THD was calculated for:

- Current (I_1)
- Current (I_2)
- Current (I_3)
- Voltage (V_{12})
- Voltage (V_{23})
- Voltage (V_{31})

These values provide an indication of waveform distortion in the system. Below is the table of the THD calculations.

Table 3.6: THD Calculations in percentage.

	$\mathbf{I_1}$	$\mathbf{I_2}$	$\mathbf{I_3}$	$\mathbf{V_{21}}$	$\mathbf{V_{32}}$	$\mathbf{V_{13}}$
a	5.71	4.80	7.56	1.46	1.66	1.95
b	5.09	3.41	6.16	1.44	1.38	1.72
c	3.59	3.53	3.76	1.51	1.49	1.54
d	5.10	5.04	8.63	1.58	1.53	1.82
e	4.90	4.01	7.05	1.61	1.48	1.77
f	3.64	3.81	3.88	1.60	1.59	1.58
g	3.53	3.48	3.43	1.48	1.42	1.51

The increase in current THD with voltage unbalance observed in Table 3.6 is consistent with the behaviour documented by von Jouanne and Banerjee [9] for adjustable speed drives. They demonstrated that under unbalanced voltage conditions, uncharacteristic harmonics, particularly triplen harmonics such as the 3rd and 9^{th}, appear in the current spectrum. In their study of a $30\,\text{kVA}$ adjustable speed drive (ASD), increasing voltage unbalance from 0.30% to 3.75% caused the 3rd harmonic component to rise dramatically from 2.1% to 83.7% of the fundamental [9]. While the current THD values in Table 3.6 are lower, this is expected for a direct-on-line induction motor compared to a converter-fed system, but the same principle of harmonic amplification under unbalance applies.

Pillay et al. [10] further explained that under unbalanced supply conditions, the negative sequence currents contribute to additional I^2R losses and increased heating. The voltage THD remains consistently low across all cases $(1.1-1.8\%)$, confirming that the current distortion originates primarily from the motor's response to unbalanced voltages rather than from supply voltage distortion itself. This observation supports the use of MCSA for fault detection, as the current spectrum contains diagnostically useful information even when the supply voltage is relatively clean.

Chapter 4: Experimental results and Harmonic evaluation

4.1 Introduction

This chapter presents the experimental results obtained from the test bench described in Chapter 2, following the signal processing methodology outlined in Chapter 3. The primary objective is to evaluate how supply voltage unbalance (introduced via the rheostat) and load level affect the harmonic content of the stator currents, with special attention to fault indicators used in Motor Current Signature Analysis (MCSA).

Seven test cases, i.e. (cases a) through g)) were considered, combining three load levels (80%, 30%, and 0% of rated torque) and three levels of voltage unbalance (90% rheostat insertion, 50% insertion, and 0% insertion, corresponding to high, moderate, and no unbalance). The voltage and current unbalance percentages for each case were already reported in Table 3.2.

In this chapter, the following harmonic components are analysed:

- The upper sideband around the fundamental supply frequency (50 Hz), given by $f_{\mathrm{UB}} = f_1(1 + 2s)$, which is one of the classic indicators of broken rotor bars (BRB) [3]. The lower sideband shows similar behaviour and is omitted for brevity.
- The 3rd, 5th, and 7th harmonics of the supply frequency (150 Hz, 250 Hz, 350 Hz), which can be associated with stator winding asymmetry, magnetic saturation, or unbalanced supply conditions [2].
- For each harmonic order, the magnitudes are reported in decibels (dB) relative to the fundamental supply harmonic (at 50 Hz and 0 dB reference). All results are derived from the stator current signals of phase 1 (I_1), phase 2 (I_2), and phase 3 (I_3).

The numerical values presented in this chapter were recorded directly from the FFT spectra of each test case. Figures 4.1 to 4.7 show the normalized current spectra for cases a through g, respectively.

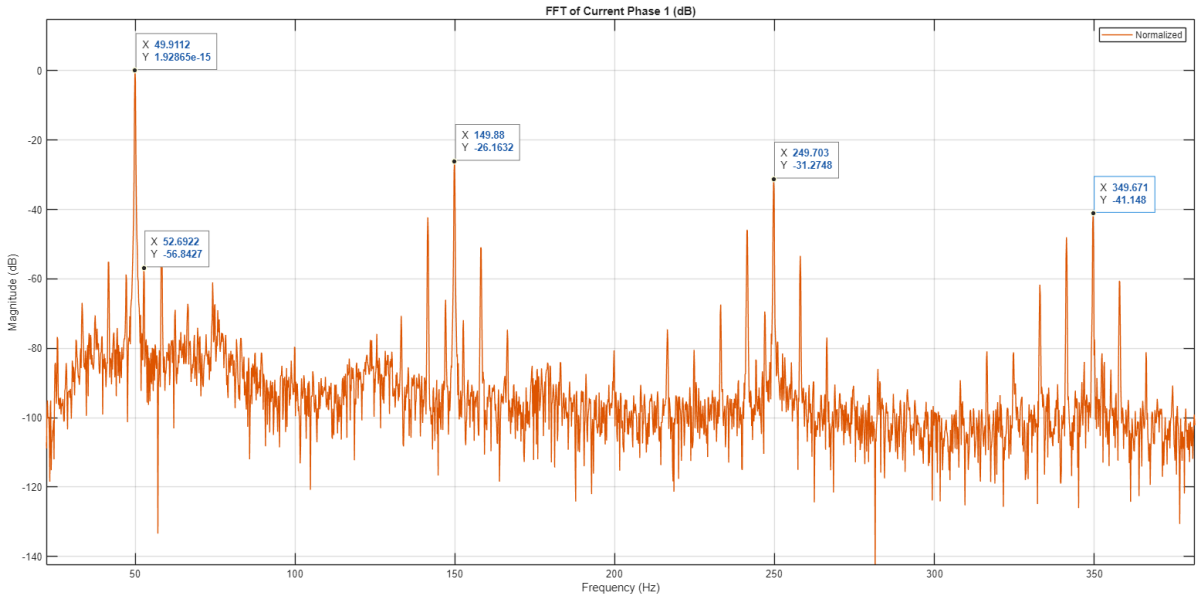

Figure 4.1: Normalised current spectrum (phase 1) case a).

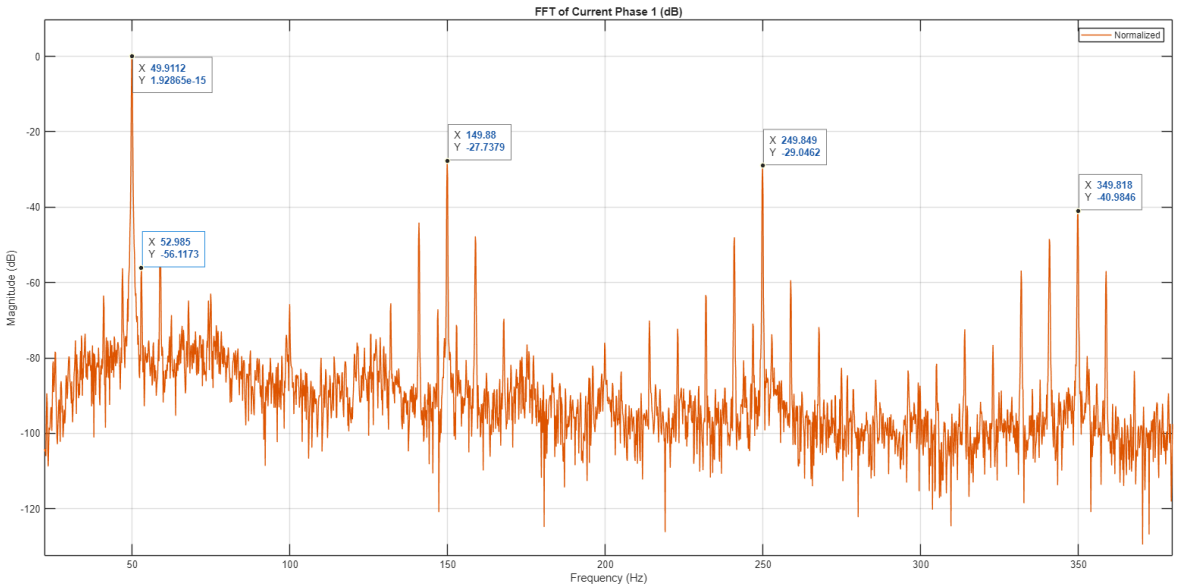

Figure 4.2: Normalised current spectrum (phase 1) case b).

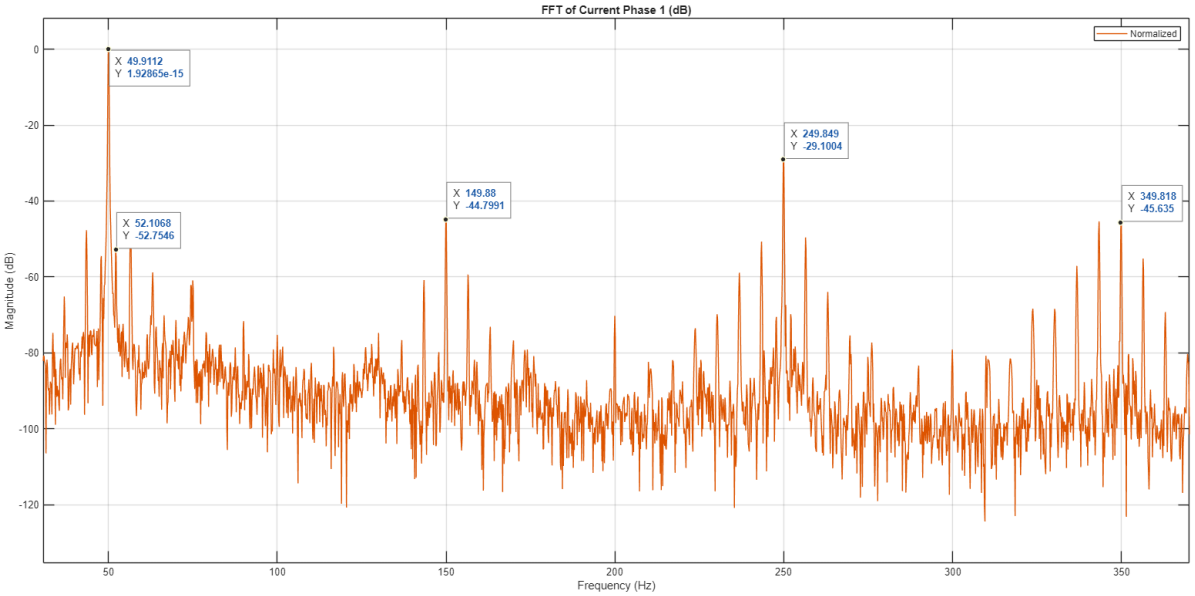

Figure 4.3: Normalised current spectrum (phase 1) case c).

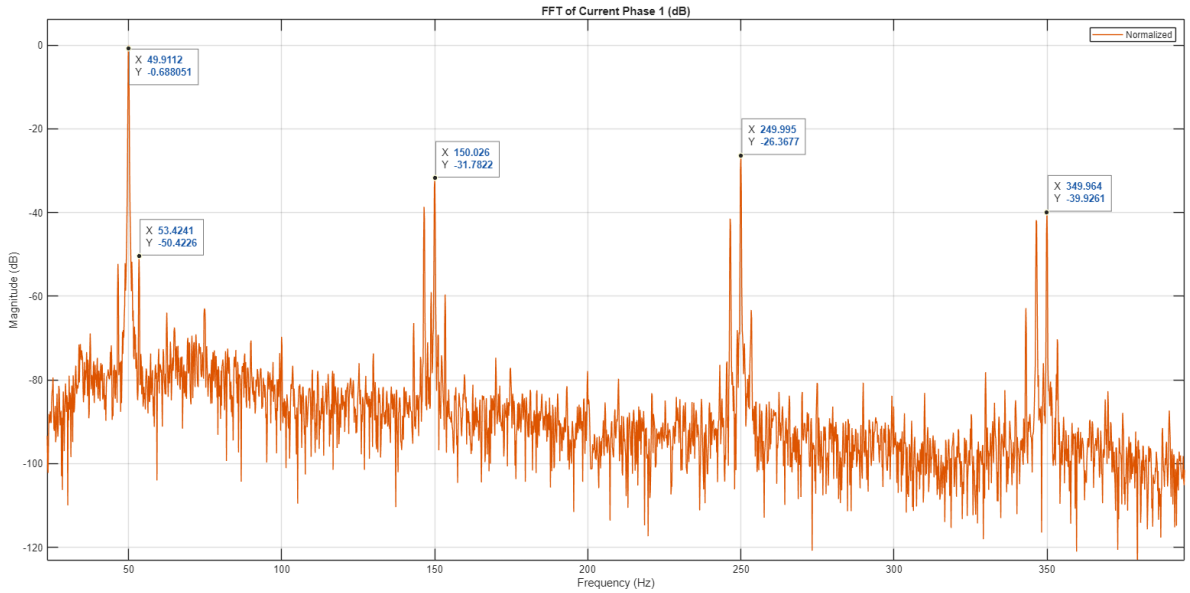

Figure 4.4: Normalised current spectrum (phase 1) case d).

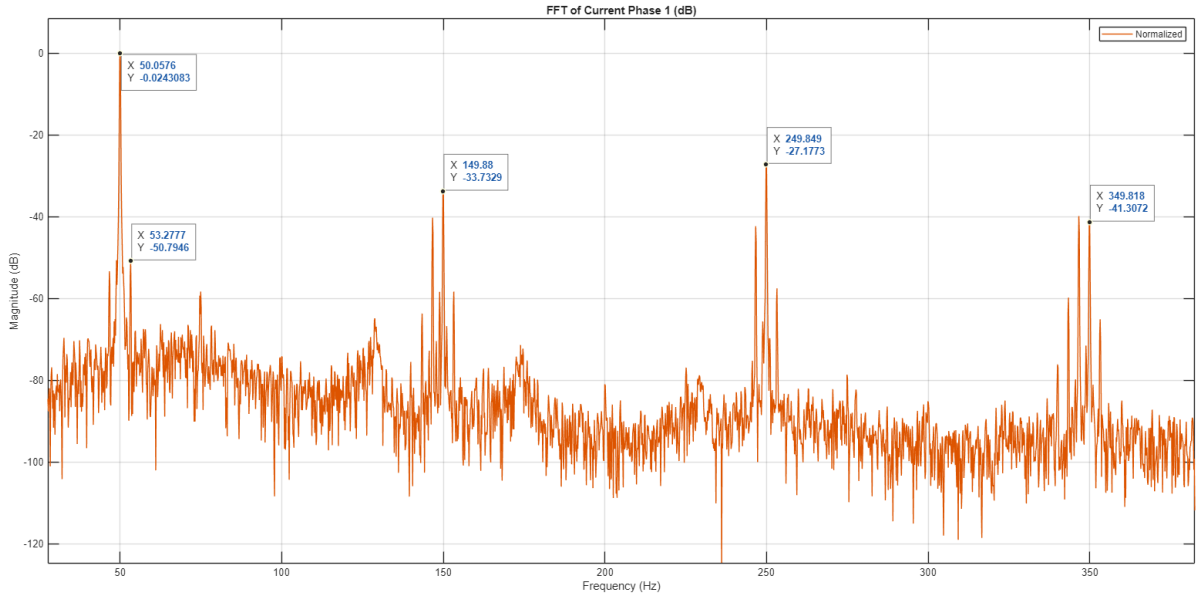

Figure 4.5: Normalised current spectrum (phase 1) case e).

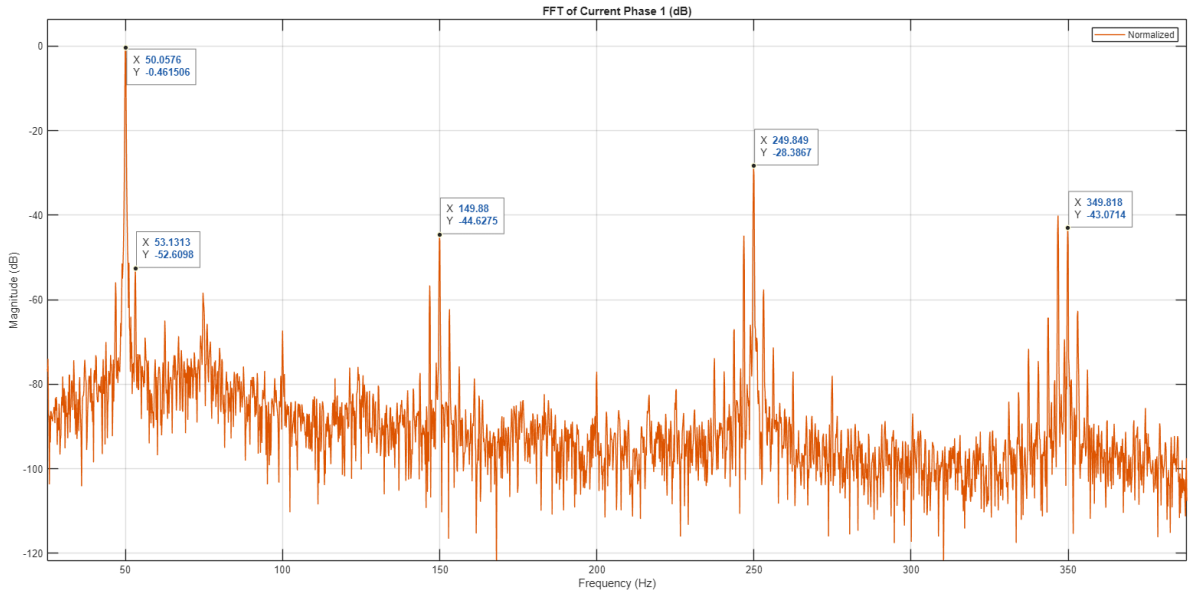

Figure 4.6: Normalised current spectrum (phase 1) case f).

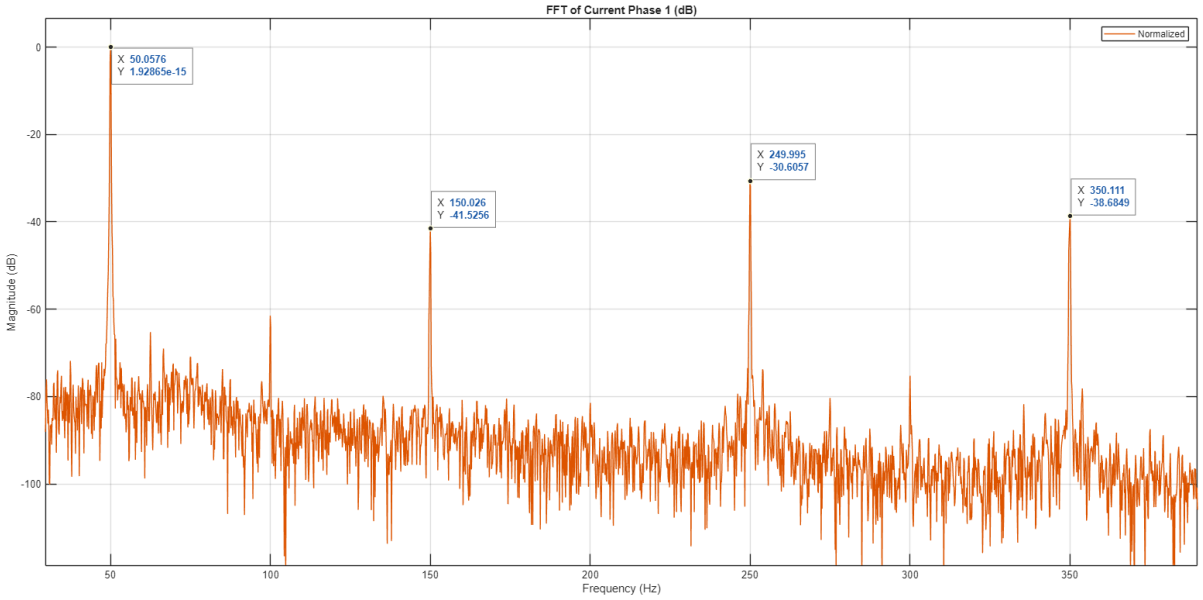

Figure 4.7: Normalised current spectrum (phase 1) case g).

At a first sight it can be noted from the figures a higher presence of harmonics and inter-harmonics in the high-loaded tests, i.e. from case a) to case c). the balanced case with no-load (case g)) presents the least "dirty" spectra (with less harmonics).

4.2 Harmonic analysis of currents

4.2.1 Broken rotor bar sideband (upper sideband around 50 Hz)

For a healthy induction motor operating under ideal conditions, the sideband magnitudes are typically very low. In their seminal study, Kliman et al. [13] reported that healthy motors exhibited a lower sideband (LSB1) of less than -60 dB relative to the fundamental component. More recent industrial guidelines suggest that sideband magnitudes approaching -45 dB to -40 dB may indicate incipient broken rotor bars, warranting further investigation [3].

Table 4.1 lists the measured upper sideband frequency and its magnitude (in dB) for each case and phase. The slip s is calculated from $f_{\mathrm{UB}} = f_1(1 + 2s)$ [3], using the measured fundamental frequency (49.91 Hz for most cases, 50.05 Hz for cases d and g).

Table 4.1: Upper sideband frequency and magnitude (dB) with calculated slip.

Case	Load	Unbalance	I_1 (dB)	I_2 (dB)	I_3 (dB)	Frequency (average between 3 phases) (Hz	s (%)
a	80%	90% R	-56.84	-57.48	-56.69	52.78	2.78
b	80%	50% R	-56.11	-56.57	-56.03	53	3.07
c	80%	0% R	-52.75	-53.19	-52.09	52.1	2.19
d	30%	90% R	-51.8	-51.9	-52.5	51.1	1.10
e	30%	50% R	-52.3	-51.9	-52.8	50.9	0.9
f	30%	0% R	-51.2	-49.1	-49.5	51.1	1.1
g	0%	0% R	Non visible	Non visible	Non visible	Non visible	-----

Some zooms of the images around the supply harmonic (in which upper slip harmonics appear) are presented in the next figures.

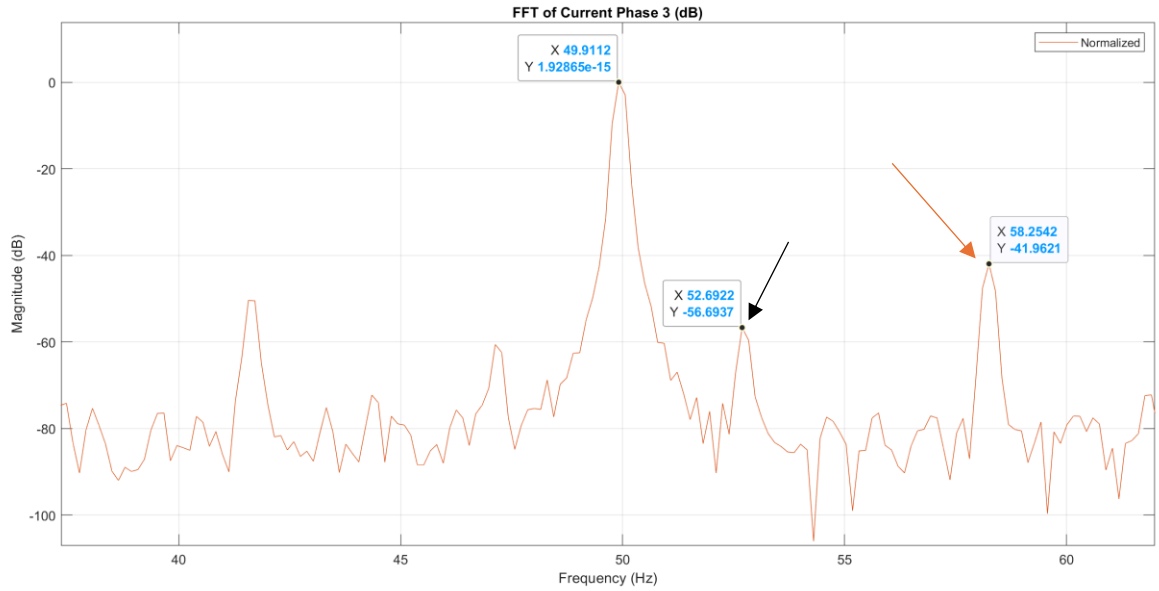

Figure 4.8: Upper slip harmonic at 80% load, faulty (90%R unbalance)- case a).

In the case of high load, the upper sideband at 52.7 Hz (indicated by the blue arrow) is well separated from the supply harmonic. Note also the appearance of another harmonic at approximately 58.3 Hz (orange arrow), probably the third harmonic of the upper slip sideband.

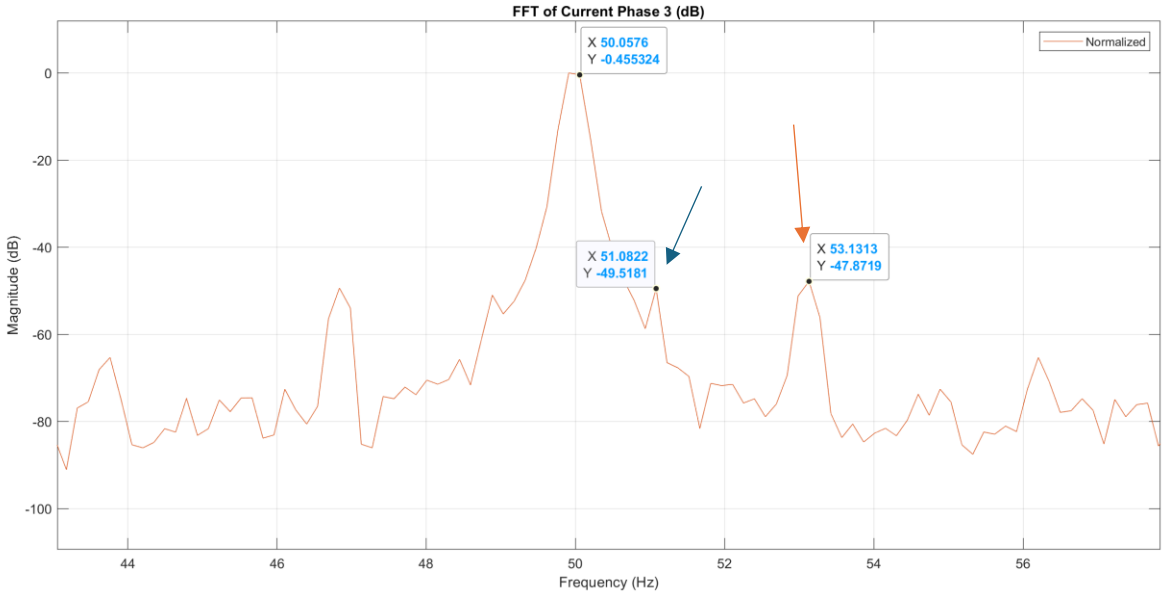

Figure 4.9: Upper slip harmonic at 30% load, healthy (no unbalance)- case f).

In the case of 30%load, the upper sideband is much closer to the supply harmonic. However, it still can be distinguished. Also, here there is a harmonic at approximately 3 times the upper slip harmonic (at 53.1 Hz), indicated by orange arrow.

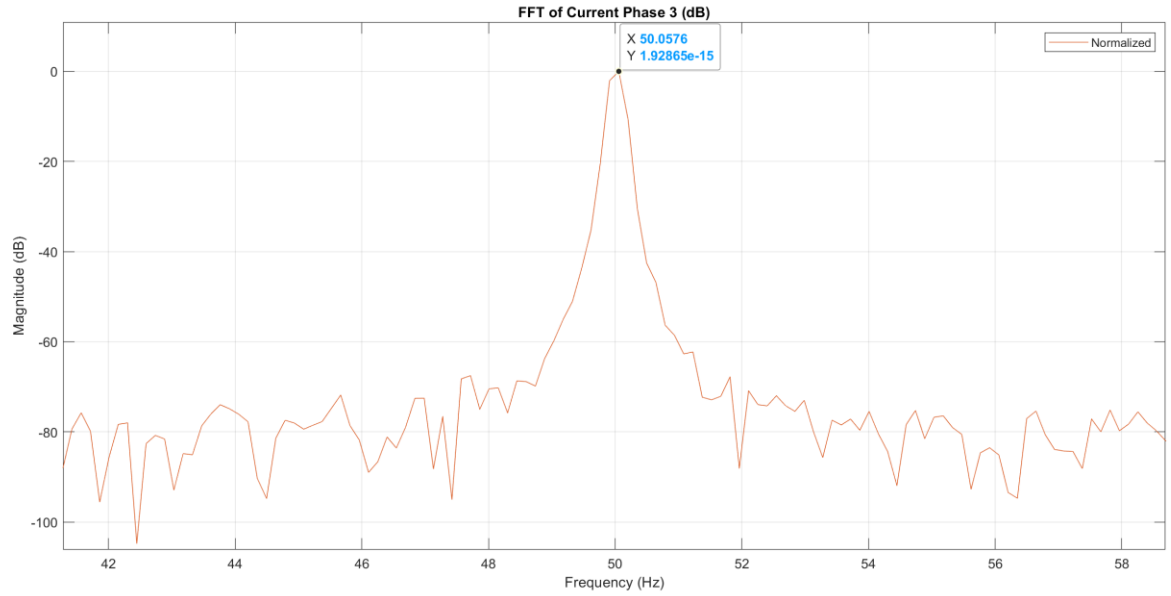

Figure 4.10: No upper slip harmonic visible at no load, no unbalance -case g)

At no load, neither the upper nor the lower slip sidebands are visible. This is widely known from literature; in fact, since the slip and the load current are very low, the sidebands are very low in amplitude and very close to the supply harmonic. For these reasons they are "buried" by the much bigger supply harmonic [18].

General observations:

- The highest (least negative) sideband magnitudes occur in cases d), e), and f), all at 30% load. Specifically, case d) I_1 at -51.80 dB, case e) I_2 at -51.90 dB, and case f) I_2 at -49.10 dB (with I_3 similarly at -49.50 dB). These values approach the typical warning range for broken rotor bars (–45 dB to –40 dB) reported in industrial MCSA guidelines [3]. However, since the motor was healthy, these elevated sidebands are likely due to the combined effect of inherent magnetic asymmetries, voltage unbalance, and light load, not actual rotor damage.
- In the balanced 80% load case (c), sidebands are around -52 dB to -53 dB, which is higher than the unbalanced cases (for all the three currents). This indicates that voltage unbalance can decrease sideband amplitude under certain conditions (high load, high unbalance). However, it must be said that the harmonic frequency is high with 90%R unbalance, increases with intermediate unbalance and then become minimum in balanced conditions.
- In the 30% load cases, the observations above are not valid: the harmonic stay stable in magnitude and frequency for all the tests.
- So, it can be said that the effect of the voltage unbalance has an influence on the slip harmonics especially at high load. The upper harmonics (but similar behaviour is observable with lower harmonic) increases its magnitude with no-unbalance. However, the frequency and then the slip is higher in unbalanced conditions.

4.2.2 3rd harmonic (150 Hz)

Table 4.2 presents the magnitude of the 3rd harmonic component (≈150 Hz) for each case and phase current, taken from the frequency-domain spectra.

Table 4.2: 3rd harmonic magnitude (dB).

Case	Load	Unbalance	I_1 (dB)	I_2 (dB)	I_3 (dB)
a	80%	90% R	-26.16	-27.44	-23.14
b	80%	50% R	-27.73	-31.39	-25.62
c	80%	0% R	-44.79	-56.72	-45.44
d	30%	90% R	-31.78	-27.03	-21.38
e	30%	50% R	-33.73	-30.45	-24.80
f	30%	0% R	-44.62	-63.61	-43.33
g	0%	0% R	-41.52	-46.48	-50.20

Observations:

- The strongest 3rd harmonic (least negative) is case d) I_3 at –21.38 dB, followed by case a) I_3 (-23.14 dB) and case e) I_3 (-24.80 dB). All correspond to unbalanced supply with both high and low load (80% or 30%). However, the third harmonic is higher in low load conditions, since even case e) -that have less unbalance – have a higher harmonic than I_1 and I_2 of the 90%R-unbalanced and high-loaded case a).
- In balanced cases (c and f), the 3rd harmonic is much weaker, e.g., case c) I_2 at (-56.72 dB), case f) I_2 at (-63.61 dB). This confirms that voltage unbalance strongly excites the 3rd harmonic, as also known from literature. It is worth nothing the variability between the three phase currents also in balanced cases: in case c) there are about 10 dB difference between minimum and maximum harmonics while in case f) more than 20 dB, that are quite a lot.
- The no-load case g) shows moderate 3rd harmonic values (-41 to -50 dB), likely due to residual magnetic asymmetry.

- Phase-to-phase variation is evident (e.g., case d: I_3 = -21.38 dB vs I_1 = -31.78 dB), showing that unbalance affects phases differently. To be noted that the third phase current I_3, is the current passing through the rheostat.

4.2.3 5th harmonic (250 Hz)

Table 4.3 gives the 5th harmonic magnitudes.

Table 4.3: 5th harmonic magnitude (dB).

Case	Load	Unbalance	I_1 (dB)	I_2 (dB)	I_3 (dB)
a	80%	90% R	-31.27	-33.39	-31.27
b	80%	50% R	-29.04	-32.50	-27.85
c	80%	0% R	-29.10	-29.20	-28.68
d	30%	90% R	-26.36	-30.70	-29.72
e	30%	50% R	-27.17	-31.80	-27.93
f	30%	0% R	-28.38	-27.93	-27.79
g	0%	0% R	-30.60	-30.45	-30.49

All 5th harmonic values lie between -26 dB and -34 dB, which is low and does not show a clear dependence on unbalance or load. This suggests that the 5th harmonic is not a sensitive indicator for the faults studied.

4.2.4 7th harmonic (350 Hz)

Table 4.4 summarises the 7th harmonic magnitudes.

Table 4.4: 7th harmonic magnitude (dB).

Case	Load	Unbalance	I_1 (dB)	I_2 (dB)	I_3 (dB)
a	80%	90% R	-41.14	-49.72	-42.37
b	80%	50% R	-40.98	-43.50	-47.07
c	80%	0% R	-45.63	-43.08	-43.94
d	30%	90% R	-39.92	-40.30	-43.53
e	30%	50% R	-41.30	-43.84	-62.04
f	30%	0% R	-43.07	-40.73	-45.08
g	0%	0% R	-38.68	-41.13	-40.54

Observations:

- Most values are between -38 dB and -49 dB, which is low and confirms that high-order harmonics are negligible.
- The highest (least negative) values occur in case g) (no-load, balanced) at -38.68 dB and -40.54 dB, and in case d) I_1 at -39.92 dB. These are still modest.
- An anomaly is observed in case e) with I_3 at -62.04 dB, which is significantly lower than the other phases in the same case. This may be due to a measurement artefact or a specific cancellation effect under the particular unbalance condition.
- It can be observed some variability between the three phase currents, more than the case of the 5th harmonic. In fact, between phase currents can be a difference of about 20 dB (case e)), or in the other cases, about 5 to 8 dB.

4.3 Comments on voltage signals

The voltage signals are also considered in this study, though usually the current signal is more considered in literature due to its higher sensibility. Generally, a qualitative assessment of the corresponding spectra is provided. However, for the lower order harmonics (the 3rd, the 5th and the 7th) quantitative analysis is carried out. Finally, some observations about some inter-harmonics are also described.

4.3.1 Harmonics analysis

The FFT results indicate that the voltage waveforms are predominantly sinusoidal, characterized by a dominant fundamental component and negligible harmonic contributions.

The harmonic content of these signals was found to be consistently minimal across all test conditions. As reported in Table 3.6, the Total Harmonic Distortion (THD) of the voltage remained within the range of 1.1% to 1.8%, indicating a high-quality voltage supply with limited harmonic distortion.

This behaviour is consistent with the expectation of a stiff voltage source, where the supply remains largely unaffected by load-induced nonlinearities. In contrast, the current waveforms are significantly influenced by the nature of the connected loads, particularly under nonlinear operating conditions. Below are some figures that show the normalized voltage spectra for cases a) through c).

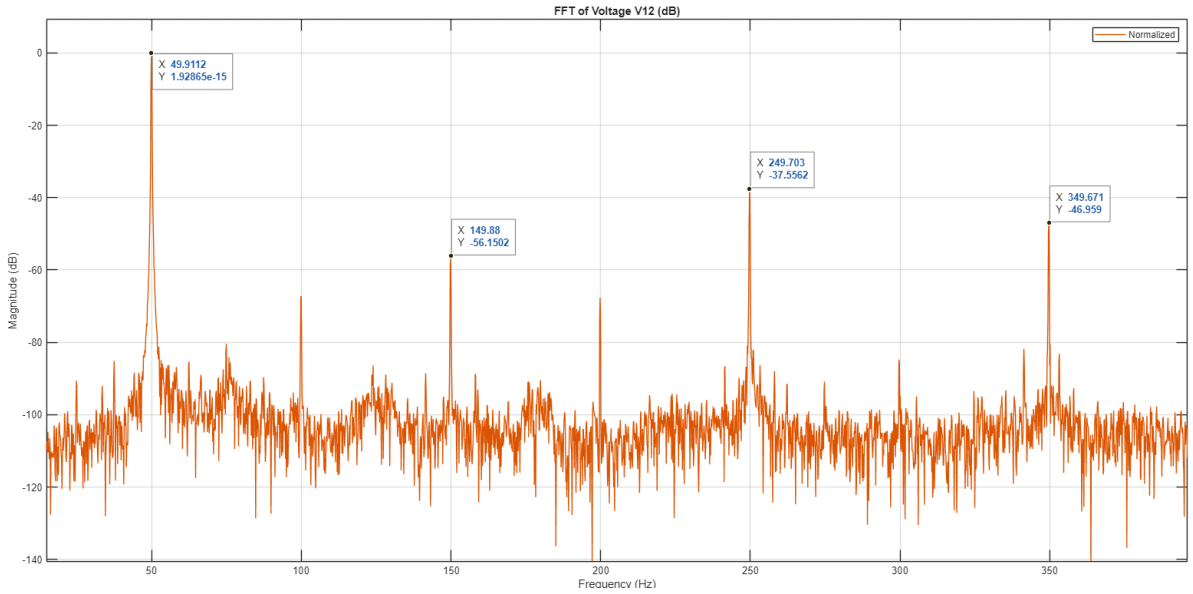

Figure 4.11: Normalised voltage spectrum (V_{12}) case a).

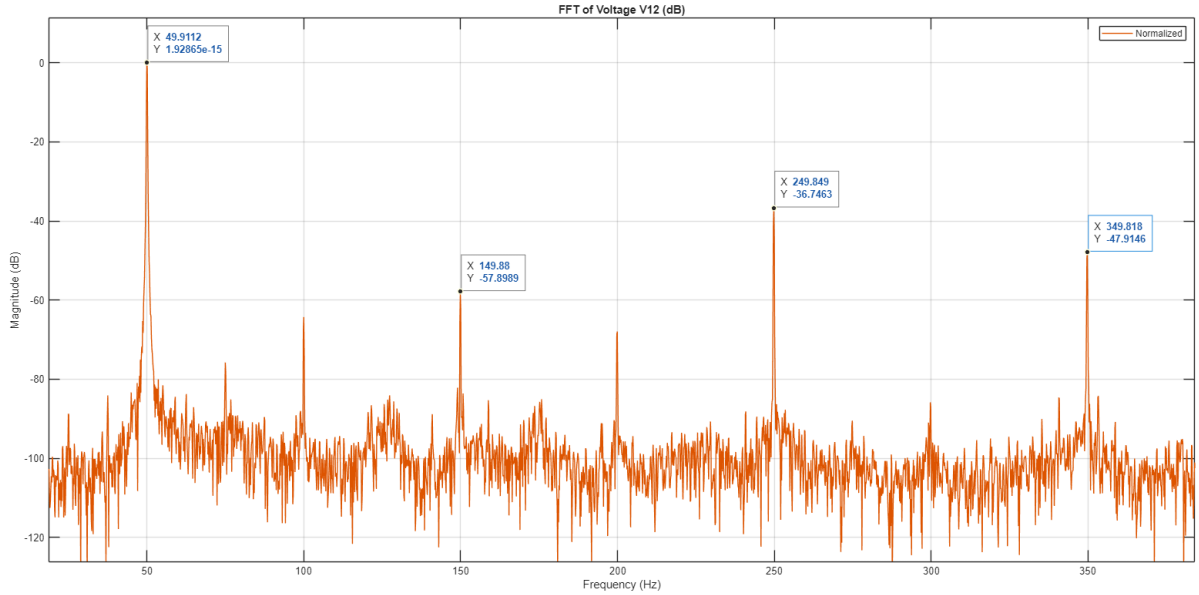

Figure 4.12: Normalised voltage spectrum (V_{12}) case b).

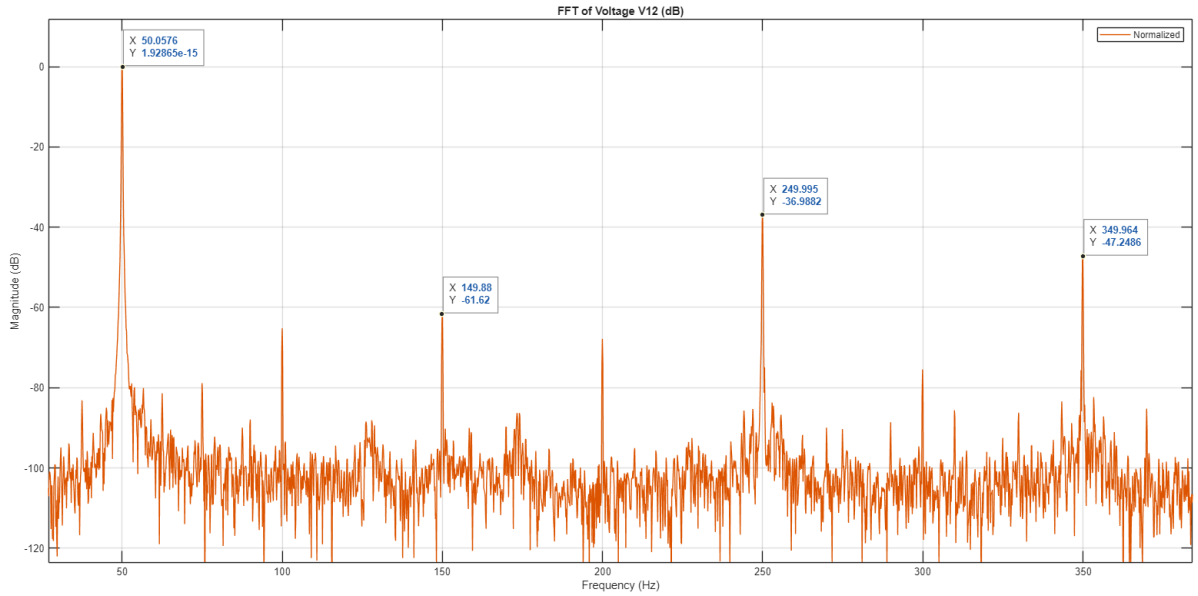

Figure 4.13: Normalised voltage spectrum (V_{12}) case c).

It can be noted from the figures (that represent the voltage V_{12}, that the third harmonic is very low (about -60 dB), while the fifth and the seventh are higher (about -36 and -47 dB, respectively). These values remain more or less constant in balanced and unbalanced conditions.

However, different observations are possible for the third harmonic in voltages V_{23} and V_{31}, as will be shown in the following.

Tables 4.7, 4.8 and 4.9 gives the 3rd, 5th and 7th harmonic magnitudes of line voltages (in dB) respectively.

Table 4.7: 3rd harmonic magnitude of line voltages (dB)

Case	Load	Unbalance	V_{12} (dB)	V_{23} (dB)	V_{31} (dB)
a	80%	90% R	-56.15	-40.12	-39.68
b	80%	50% R	-57.89	-46.11	-44.94
c	80%	0% R	-61.62	-62.06	-67.62
d	30%	90% R	-59.79	-43.73	-42.32
e	30%	50% R	-58.42	-54.11	-49.67
f	30%	0% R	-58.77	-60.39	-64.82
g	0%	0% R	-58.80	-59.42	-63.95

Table 4.8: 5th harmonic magnitude of line voltages (dB)

Case	Load	Unbalance	V_{12} (dB)	V_{23} (dB)	V_{31} (dB)
a	80%	90% R	-37.55	-39.01	-36.44
b	80%	50% R	-36.74	-38.20	-35.66
c	80%	0% R	-36.98	-37.31	-36.91
d	30%	90% R	-35.99	-37.54	-35.40
e	30%	50% R	-36.35	-37.42	-35.68
f	30%	0% R	-35.97	-36.26	-36.06
g	0%	0% R	-39.03	-39.40	-39.02

Table 4.9: 7th harmonic magnitude of line voltages (dB)

Case	Load	Unbalance	V_{12} (dB)	V_{23} (dB)	V_{31} (dB)
a	80%	90% R	-46.95	-44.58	-46.82
b	80%	50% R	-47.91	-47.29	-48.17
c	80%	0% R	-47.24	-47.74	-49.13
d	30%	90% R	-44.51	-44.68	-46.15
e	30%	50% R	-47.65	-48.75	-48.45
f	30%	0% R	-44.83	-46.05	-47.34
g	0%	0% R	-43.36	-44.94	-44.08

It can be noted from tables 4.8 and 4.9 (regarding 3rd and 5th harmonics) that the magnitudes remain almost constant in all the cases and voltages considered. However, form table 4.7 (regarding the 3rd harmonic), it can be seen a behaviour difference between voltage V_{12} and voltages V_{23} and V_{31}. In fact, while V_{12} remain constant in the various cases, the other two voltages have variability from unbalanced to balanced cases. From the most unbalanced cases to the balanced ones the third harmonics decrease of about 20 dB. This is less than what appear in current signals (in which about 30 dB differences are recorded), but it is still considerable. To the sake of clarity, the voltage V_{23} in case b) is reported in the next Figure 4.14.

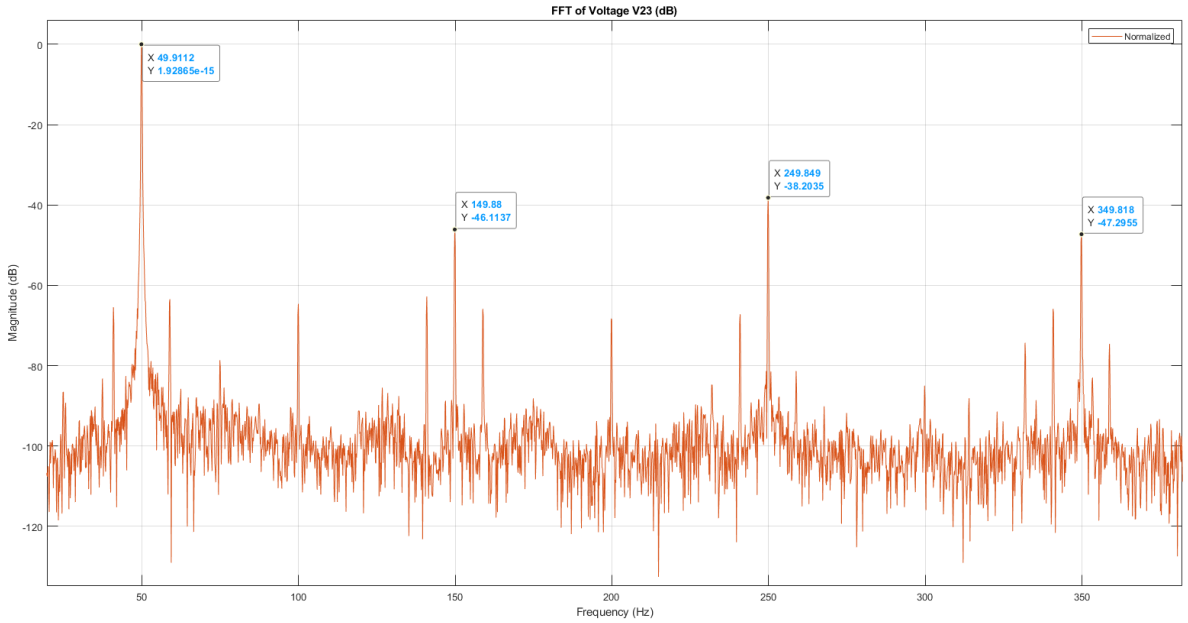

Figure 4.14: Normalised voltage spectrum (V_{23}) case b).

Note that the unbalance resistor is inserted in phase 3. So, since both voltage V_{23} and V_{31} include the flawed phase-voltage E_3 (line voltages are calculated as differences of two-phase voltages) it can be assumed that the third harmonic change in these voltages is directly correlated to this fault. This method so, could help also to localize the fault (a high resistance connection on one phase).

4.3.2 Inter-harmonics analysis

It is worth noting that also the sideband harmonics around the supply harmonic in the voltage signals change from the three line-line voltages taken.

For example, in the unbalanced cases, the sidebands at about $f_s \pm 6s \cdot f_s$ are visible in current and voltage signals except for the signal V_{12}. For the same reason discussed about the third harmonic, these sidebands could be correlated to the voltage unbalance since both voltages V_{23} and V_{31} include the flawed phase-voltage E_3 while V_{12} doesn't.

The next images show these harmonics for cases d), e) and f) in current and voltage signals (represented together). Note that the spectra are presented non-normalized to avoid graphic super-positions.

Completely similar results are observed for the high-loaded cases a), b) and c), however, they are omitted for brevity.

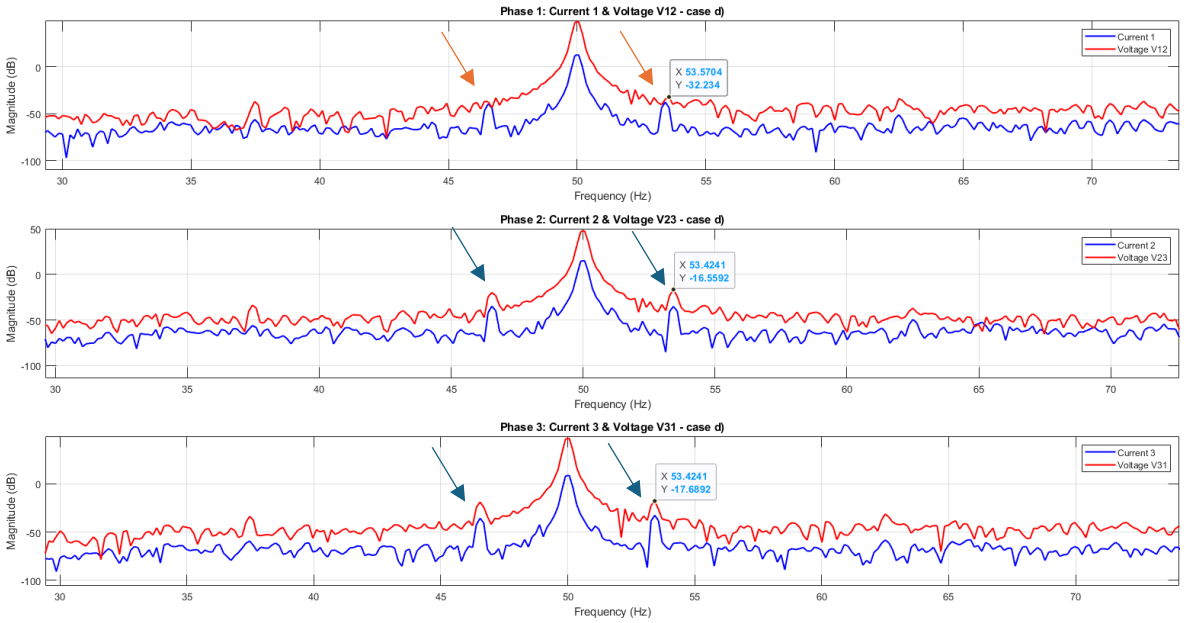

Figure 4.15: ($f_s \pm 6s \cdot f_s$) sidebands in the balanced case d): very visible for V_{23} and V_{31} (blue arrows) but not visible for V_{12} (orange arrows)

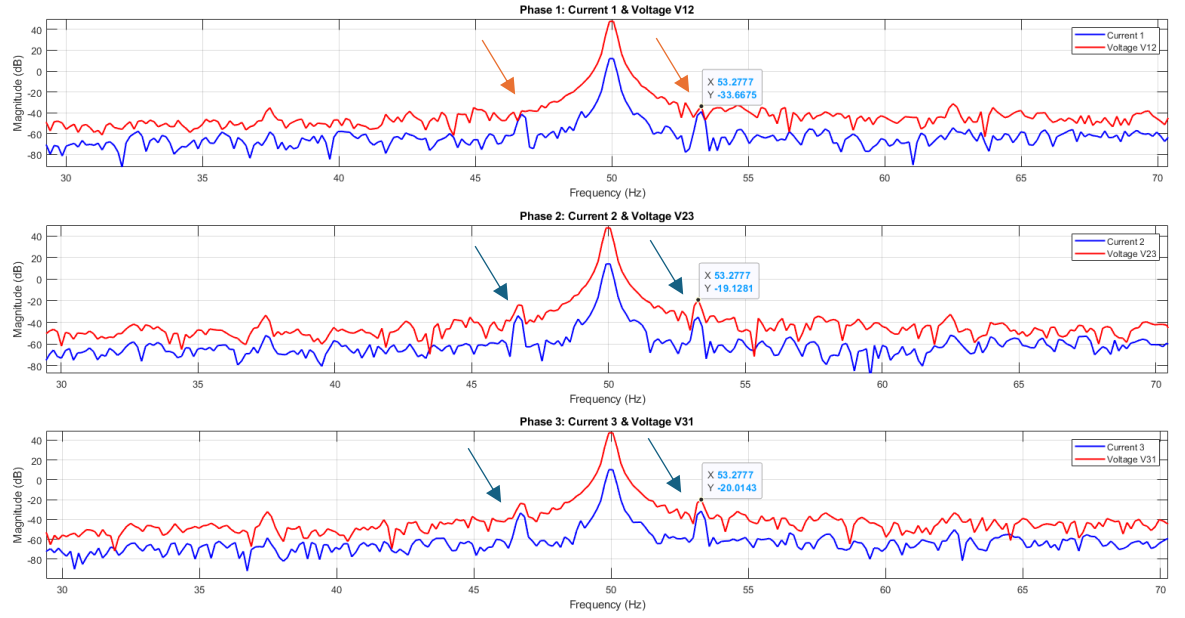

Figure 4.16: ($f_s \pm 6s \cdot f_s$) sidebands in case e): quite visible for V_{23} and V_{31} (blue arrows) but not visible for V_{12} (orange arrows)

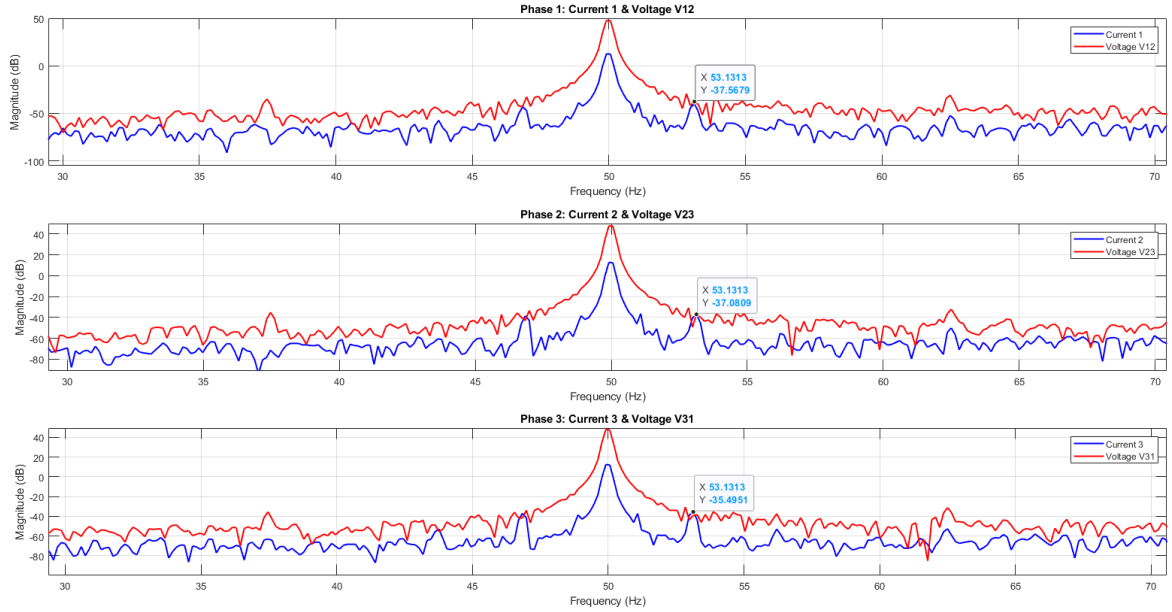

Figure 4.17: ($f_s \pm 6s \cdot f_s$) sidebands in the balanced case f): the sidebands are visible only in the current signals.

Further studies can be conducted to verify and validate the method. However, it is important to highlight that this method (and the method based on the third harmonic) could be implemented both to diagnose -but also to localize- the presence of the unbalance (on which phase there is the unbalance).

Conclusion

This thesis investigated the effects of supply voltage unbalance on the behaviour of three-phase induction motors, with particular emphasis on its impact on harmonic components used in Motor Current Signature Analysis (MCSA). The study combined theoretical analysis, experimental investigation, and signal processing techniques to evaluate how unbalanced operating conditions influence diagnostic indicators.

A dedicated experimental test bench was developed to reproduce controlled operating scenarios, including different load levels and degrees of voltage unbalance. The integration of a magnetic powder brake allowed precise load control, while the use of a rheostat enabled the introduction of repeatable and adjustable unbalance conditions. Electrical quantities were acquired using both conventional measurement systems and an advanced digital circuit breaker, demonstrating the feasibility of combining protection and monitoring functionalities within a single device.

The signal processing methodology implemented in MATLAB proved effective in extracting meaningful information from the measured data. Time-domain analysis provided an initial qualitative assessment, while frequency-domain analysis using FFT enabled the identification and quantification of harmonic components. The use of normalization and decibel representation allowed a clear comparison between different test conditions.

The experimental results highlighted several important findings. Among the analysed harmonics, the third harmonic component of the stator current was found to be highly sensitive to voltage unbalance, showing a significant increase in magnitude under unbalanced conditions. This confirms its suitability as a reliable indicator of supply asymmetry. In contrast, the fifth and seventh harmonics exhibited relatively low sensitivity, suggesting a limited diagnostic value for the specific conditions investigated. Phase to phase variations in harmonic magnitudes has been also identified.

A particularly valuable outcome of this work is the observation that voltage harmonic components, especially the third harmonic in line voltages, can provide useful information not only for fault detection but also for fault localization. The different behaviour observed between line voltages allowed the identification of the affected phase, highlighting a potential extension of traditional MCSA techniques.

Overall, the results demonstrate that voltage unbalance has a significant impact on harmonic signatures and must be carefully considered when applying MCSA for fault diagnosis. Neglecting this effect may lead to misinterpretation of diagnostic indicators and incorrect assessment of machine health.

Future work can extend this research in several directions. First, additional experiments could be conducted on motors with actual faults, such as broken rotor bars or stator winding defects, to evaluate the combined effects of faults and voltage unbalance. Second, advanced signal processing techniques, including time-frequency analysis or machine learning algorithms, could be applied to improve diagnostic accuracy and robustness. Finally, further development

of integrated monitoring systems based on digital circuit breakers could enable real-time, industrial-scale implementation of these diagnostic methods.

Bibliography

[1] S. B. Lee et al., "Condition monitoring of industrial electric machines: State of the art and future challenges," *IEEE Ind. Electron. Mag.*, vol. 14, no. 4, pp. 158-167, Dec. 2020.

[2] I. Temiz, C. Akuner, and H. Calik, "Analysis of Balanced Three-Phase Induction Motor Performance under Unbalanced Supply using Simulation and Experimental Results", Electronics and Electrical Engineering, no. 3(109), pp. 41-45, 2011.

[3] W. T. Thomson and R. J. Gilmore, "Motor Current Signature Analysis to Detect Faults in Induction Motor Drives—Fundamentals, Data Interpretation, and Industrial Case Histories," *Proceedings of the Thirty-Second Turbomachinery Symposium*, 2003.

[4] ABB, "Unbalanced voltage supply: The damaging effects on three phase induction motors and rectifiers," ABB White Paper, 2015.

[5] A. Khoobroo, M. Krishnamurthy, B. Fahimi, and W. J. Lee, "Effects of System Harmonics and Unbalanced Voltages on Electromagnetic Performance of Induction Motors," in *IEEE International Electric Machines & Drives Conference (IEMDC)*, 2009.

[6] H. de Swardt, “Wedge failures on LV mush-wound motors,” *Technical Report*, Nov. 2003

[7] MAGTROL Magnetic Powdered Dynamometer User’s Manual

[8] ABB, “Three-Phase Voltage Imbalances,” ABB, Document LVD-EOTKN113U-EN REV A, Nov. 22, 2022.

[9] A. von Jouanne and B. Banerjee, "Assessment of voltage unbalance," in *IEEE Transactions on Power Delivery*, vol. 16, no. 4, pp. 782-790, Oct. 2001, doi: 10.1109/61.956770.

[10] P. Pillay, P. Hofmann and M. Manyage, "Derating of induction motors operating with a combination of unbalanced voltages and over or undervoltages," in *IEEE Transactions on Energy Conversion*, vol. 17, no. 4, pp. 485-491, Dec. 2002.

[11] Manuel Marzitelli “Investigations on online condition monitoring of induction motors with a digital programmable protection unit moulded-case circuit breaker”, Master Thesis In Industrial Automation Engineering, University of Pavia, A.Y. 2023-2024.

[12] https://fiveable.me/electrical-circuits-systems-ii/unit-6/balanced-unbalanced-three-phase-power-calculations/study-guide/H81a3MS5nCKGguzR [accessed March 2026]

[13] G. B. Kliman, R. A. Koegl, J. Stein, R. D. Endicott, and M. W. Madden, "Noninvasive detection of broken rotor bars in operating induction motors," *IEEE Trans. Energy Convers.*, vol. 3, no. 4, pp. 873–879, Dec. 1988.

[14] M. Minervini, L. Mantione, L. Frosini, P. Giangrande and F. Muzio, "Induction Motor Low Frequency Torque Oscillation Diagnostics Through Circuit Breaker Acquisitions," 2025 IEEE Symposium on Diagnostics for Electric Machines, Power Electronics and Drives (SDEMPED), Dallas, TX, USA, 2025, pp. 1-7, doi: 10.1109/SDEMPED53223.2025.11154358.

[15] C. L. Fortescue, "Method of symmetrical coordinates applied to the solution of polyphase networks," *AIEE Transactions*, vol. 37, no. 2, pp. 1027-1140, 1918.

[16] IEC 60034-26:2026, *Rotating electrical machines – Part 26: Effects of unbalanced voltages on the performance of three-phase cage induction motors*, International Electrotechnical Commission, Geneva, Switzerland, 2026.

[17] NEMA MG 1, *Motors and Generators*, National Electrical Manufacturers Association, Rosslyn, VA, USA.

[18] F. Vedreno-Santos, J. Martinez-Roman, R. Puche-Panadero, and M. Pineda-Sanchez, "Diagnosis of rotor asymmetries in induction motors: A steady state approach using rotating frame references," *Measurement: Sensors*, vol. 33, art. no. 101234, 2025.

[19] K. N. Gyftakis, M. Salinas, N. Trachalakis, et al., "Zero-sequence flux analysis aiming for reliable detection of broken rotor bars in induction motors," *IEEE Transactions on Industry Applications*, early access, 2025. doi: 10.1109/TIA.2025.3542100.

[20] H. G. Beleiu, S. G. Pavel, I. M. T. Birou, et al., "Effects of voltage unbalance and harmonics on drive systems with induction motor," *Journal of Engineering Research*, vol. 10, no. 4A, pp. 381-391, 2022.